

Near equilibrium dynamics and one-dimensional spatial-temporal structures of polar active liquid crystals*

Yang Xiao-Gang(杨小刚)^{a)†}, M. Gregory Forest^{b)‡}, and Wang Qi(王奇)^{a)c)d)§}

^{a)}School of Mathematical Sciences, Nankai University, Tianjin 300071, China

^{b)}Department of Mathematics, University of North Carolina at Chapel Hill, Chapel Hill, NC 27599-3250, USA

^{c)}Department of Mathematics, Interdisciplinary Mathematics Institute and NanoCenter at USC, University of South Carolina, Columbia, SC 29028, USA

^{d)}Beijing Computational Science Research Center, Beijing 100083, China

(Received 29 May 2014; published online 24 September 2014)

We systematically explore near equilibrium, flow-driven, and flow-activity coupled dynamics of polar active liquid crystals using a continuum model. Firstly, we re-derive the hydrodynamic model to ensure the thermodynamic laws are obeyed and elastic stresses and forces are consistently accounted. We then carry out a linear stability analysis about constant steady states to study near equilibrium dynamics around the steady states, revealing long-wave instability inherent in this model system and how active parameters in the model affect the instability. We then study model predictions for one-dimensional (1D) spatial-temporal structures of active liquid crystals in a channel subject to physical boundary conditions. We discuss the model prediction in two selected regimes, one is the viscous stress dominated regime, also known as the flow-driven regime, while the other is the full regime, in which all active mechanisms are included. In the viscous stress dominated regime, the polarity vector is driven by the prescribed flow field. Dynamics depend sensitively on the physical boundary condition and the type of the driven flow field. Bulk-dominated temporal periodic states and spatially homogeneous states are possible under weak anchoring conditions while spatially inhomogeneous states exist under strong anchoring conditions. In the full model, flow-orientation interaction generates a host of planar as well as out-of-plane spatial-temporal structures related to the spontaneous flows due to the molecular self-propelled motion. These results provide contact with the recent literature on active nematic suspensions. In addition, symmetry breaking patterns emerge as the additional active viscous stress due to the polarity vector is included in the force balance. The inertia effect is found to limit the long-time survival of spatial structures to those with small wave numbers, i.e., an asymptotic coarsening to long wave structures. A rich set of mechanisms for generating and limiting the flow structures as well as the spatial-temporal structures predicted by the model are displayed.

Keywords: active liquid crystals, active particles, spatial-temporal structures, spontaneous flows

PACS: 87.10.Ed, 87.23.Cc, 87.23.Kg

DOI: 10.1088/1674-1056/23/11/118701

1. Introduction

Active materials are driven out of equilibrium by an energy input at the microscopic scale via biological or catalytic activities. In the non-equilibrium state, some emergent spatial-temporal structures may result, such as long-range order, anomalous fluctuations, spontaneous flows, and dynamical spatial-temporal structures and patterns.^[1–11] When coupled with regulatory signaling pathways, active materials can serve as models for living systems, such as cortical layers in the cytoskeleton of cells and bacterial colonies in bacterial biofilms.^[12–16]

Active particles are generally anisotropic in their configuration and motion and can form self-assembled ordered states with respect to orientation and motion.^[17,18] The nature of the ordered state depends on both the configuration of the individual particles and interactions among the particles. Ac-

tive liquid crystals are a class of active materials with these features, which may form liquid crystalline phases at sufficiently high particle concentrations or under strong particle-particle interactions.^[19,20] When the particles possess a distinctive head and tail, the particle-fluid system is called a polar active liquid crystal, including: bacterial suspensions, asymmetric vibrated granular rods, polarized migrating cells, and catalytic charged nano-particles. Polar active particles are often modeled as self-propelled particles, where the activity is incorporated via a self-propelled velocity of individual particles. The self-propelled particle and host fluid matrix interaction is characterized by an active bulk stress. Additional particle-particle interaction can also contribute to hydrodynamics via an additional active viscous stress. In addition, when the active particle demonstrates a head-tail symmetry in its configuration, the active liquid crystal system is called

*Project supported by the National Natural Science Foundation of China (Grant Nos. DMS-1200487, DMR-1122483, and NIH 2R01GM078994-05A1), the Air Force Office of Scientific Research (AFOSR) (Grant No. FA9550-12-1-0178), and the Army Research Office (Grant Nos. ARO-12-60317-MS and SC EPSCoR GEAR (CI and CRP)).

†E-mail: nkyxg@mail.nankai.edu.cn

‡E-mail: forest@unc.edu

§Corresponding author. E-mail: qwang@math.sc.edu

© 2014 Chinese Physical Society and IOP Publishing Ltd

<http://iopscience.iop.org/cpb> <http://cpb.iphy.ac.cn>

an apolar liquid crystal. This system is also referred to as the shaker in some literature, where nematic steric interaction may be more important.^[21,22] The nature of the particle–particle interaction is crucial in determining the properties of the ordered state. Polar particles may experience either polar interactions (i.e., the ones that tend to orient particles head to head and tail to tail) or interactions that are apolar (i.e., those that orient particles regardless of their polarity), or both.^[23,24]

The polar active liquid crystal can order in polar states, as described by a nonzero vector order parameter and the mean motion. The vector order parameter is often referred to as the polarity vector or polar order parameter, whose magnitude measures the strength of the polarity. Apolar active particles generally experience apolar interactions and the resulting ordered state has the symmetry of nematic liquid crystals, where a vector order parameter that is invariant under head-tail reflection, or a second-order tensor order parameter, can be employed to describe the broken symmetry.^[19,24] There is a class of active liquid crystals with nematic symmetry at large scales that consists of self-propelled particles (hence, it is polar at the micro scale) with apolar steric interactions or hydrodynamic coupling. Such a system includes swimmers in a bulk suspension.^[25,26] These interactions lead to large-scale nematics with weak or no polar order.^[27,28] For this class of active liquid crystals, a vector order parameter along with a tensor order parameter form the minimal set of order parameters to describe the broken symmetry of the active material system.^[18] This class of active liquid crystals includes gliding myxobacteria, suspensions of auto-catalytic Janus colloids, and motile epithelial cells.^[29,30] It therefore represents an important class of active systems of direct physical relevance.

A useful theoretical framework for describing the collective behavior of the active systems is the continuum model, which generalizes liquid crystal hydrodynamics to include new activities or nonequilibrium mechanisms due to the microscopic energy input.^[19] For polar active liquid crystals, continuum models use a single vector to describe the broken symmetry.^[17,18,31] For apolar active liquid crystals, either a single vector with reflection symmetries enforced or a second order tensor with the built-in reflection symmetry can be employed to describe the broken symmetry. For more general active liquid crystals whose active particles are primarily polar while the interactions may be dominated by apolar interactions, both a single vector and a second order tensor order parameter are required to describe the broken symmetry.^[24] In these continuum models, sources of activities are implemented as low order perturbations to the corresponding passive liquid crystal systems, on which the new models are extended.^[13,16,18,19,32] A more detailed theoretical description of the active liquid crystals is the phase space or configurational space kinetic theory pioneered by Marchetti and Liverpool and Shelley *et al.*, and extended by Forest *et al.*^[18,33–40]

In this formulation of models for active liquid crystals, microscopic scale symmetry is tacitly incorporated through the interaction potential, self-propelled velocity, as well as phenomenological active forces.^[41] This formulation can unify all of the three types of continuum models through careful attention to closure procedures. For detailed reviews on the mathematical models of active materials, please refer to recent excellent review papers.^[17,18]

The emergent spatial–temporal structures in active liquid crystals are predominantly driven by instabilities, leading to an apparent departure from equilibrium states.^[33,42,43] These instabilities can sustain macroscopic global structures in time and space, as well as transient defective structures,^[13,44,45] providing an excellent model system. In reality, many active materials are exposed in a fixed domain where the boundary that confines the active material system may affect the internal dynamics. Several groups have studied active liquid crystal systems in confined geometries, revealing some interesting mechanisms for generating spontaneous flows.^[46–49] Numerical simulations for spatial–temporal patterns in two-dimensional or three-dimensional (2D or 3D, respectively) have been largely done with a periodic boundary condition.^[25,33–36,40,50] All of these works considered only the bulk active stress, some of which included the self-propelled velocity. In this paper, we extend these studies to include the active viscous stress.

We adopt and generalize a minimal polar active liquid crystal model that was developed by Marchetti *et al.*^[18,45] We study the linear stability of the constant steady states of the model with the following three active mechanisms included: bulk active stress, active viscous stress, and the self-propelled velocity. We conclude this study by providing a complete phase diagram in the parameter space of the active parameters together with a geometric parameter of the liquid crystal molecule. This study reveals the inherent instability in the model for ALC systems subject to periodic boundary conditions, which suppresses the effects of physical boundaries, and yet still reveals the lengthscales and timescales involved in the instabilities. We then explore the one-dimensional (1D) structure in a limiting regime of the model where the viscous stress dominates. In this study, we focus on two special flow fields: a linear plane shear and a nonlinear Poiseuille flow. We explore the driven dynamics of the ALC system with respect to various anchoring boundary conditions and the impact of the active mechanisms in the model. Finally, we demonstrate various 1D spatial–temporal structures in a long channel subject to various boundary conditions and show how a molecular configuration coupled with the activity mechanisms can impact the long-time behavior of these spontaneously generated flow structures. These studies reveal some new phenomena described by this model which are worthy of further detailed investigation.

This paper is organized as follows. Firstly, we will present the minimal polar liquid crystal model, following a systematic derivation which identifies the Ericksen stress and energy dissipation explicitly. Secondly, we carry out a linear stability analysis of constant steady states to study the near (hydrodynamic) equilibrium dynamics and to demonstrate the long-wave instability inherent in this model system and to find how this depends on the model parameters. Thirdly, we study model predictions in the viscous dominated regime for the active liquid crystal in 1D spatial direction while homogeneous in the other 2D subject to physical boundary conditions. Finally, we explore the model prediction for 1D spatial-temporal structures in the full model.

2. A mathematical model for polar active liquid crystals

We derive systematically a model for solutions of polar active liquid crystals (PALC), extending that proposed by Kruse *et al.*^[13,14] and Marchetti *et al.*^[49] The hydrodynamic equations for passive liquid crystal systems were systematically derived by Martin, Parodi, and Pershan, Ericksen and Leslie based on a generalized hydrodynamic approach close to equilibrium, where a unit vector is used to describe the average molecular orientation at a material point.^[20,51–53] The model we extend here allows the vector that describes the molecular orientation to vary in its length, so that it can be used to describe the defect phase, where the length is zero at the defect core, in addition to the liquid crystal phase. It clearly identifies the Ericksen stress and other elastic stresses, such that the resulting hydrodynamic model is dissipative and obeys an energy law in the absence of microscopic energy-generating activities. The mechanisms of energy-generating activities highlight the departure of the model from energy dissipation.

We assume that the active liquid crystal in the solution is polar, as described by the polarity vector \mathbf{p} . This is common in many active liquid crystal systems. For instance, the actin filament exhibits macroscopic polarity described by the front and the barbed end, swimming rodlike viruses have a polarity defined by their self-propelled velocity, flocks of birds show polarity by each individual bird's flying velocity, and bacterial movement in biofilms demonstrates a directed motion, which defines the polarity. In a coarse-grained or macroscopic description of the active liquid crystal system, we adopt the polarity vector as a macroscopic measure to describe an average polar order or self-propelled velocity field. The way that we derive the continuum model for the ALC system follows the work of Jülicher *et al.*,^[15] in which we derive the passive components of the model separately from those of the active components.

2.1. Governing system of equations

For the polar active liquid crystal system, we introduce the system free energy, as follows:

$$F = \int_V f(\mathbf{p}, \nabla \mathbf{p}) d\mathbf{x}, \quad (1)$$

where f is the free energy density per unit volume and V is the material volume. We consider the material system consisting of active liquid crystals that are self-propelled in the host fluid matrix, known as the solvent. The motion of the material system is described by the average velocity field \mathbf{v} . With respect to this velocity field, the strain rate tensor is denoted by $\mathbf{D} = (\nabla \mathbf{v} + \nabla \mathbf{v}^T)/2$ and the vorticity tensor by $\mathbf{\Omega} = (\nabla \mathbf{v} - \nabla \mathbf{v}^T)/2$. (Here, we denote $(\nabla \mathbf{v})_{\alpha\beta} = \partial_\alpha v_\beta$.) The active liquid crystal solution is assumed to be driven out of equilibrium by a constant chemical potential difference $\Delta\mu$ between ATP and its hydrolysis products.

The transport equation for the polarity vector is postulated as follows, extending the Ericksen–Leslie theory for liquid crystals^[18]

$$\frac{\partial \mathbf{p}}{\partial t} + (\mathbf{v} + \boldsymbol{\omega} \mathbf{p}) \cdot \nabla \mathbf{p} + \mathbf{\Omega} \cdot \mathbf{p} = \frac{1}{\gamma} \mathbf{h} + \lambda \Delta \mu \mathbf{p} + \nu \mathbf{D} \cdot \mathbf{p}, \quad (2)$$

where $\boldsymbol{\omega}$ together with \mathbf{p} describes the self-propelled velocity for the active liquid crystal molecule, γ is a relaxation parameter, λ characterizes how much ATP production impacts on the particle's self-propelled motion, ν is the geometrical or tumbling parameter for the liquid crystal molecule (i.e., the liquid crystal is rodlike if $\nu > 0$ and disklike if $\nu < 0$), and \mathbf{h} is the molecular field given by the variation $\mathbf{h} = -\delta F / \delta \mathbf{p}$. These parameters could depend on the density of the active liquid crystals but they are assumed to be constant in this simplified model.

The variation of the free energy is given by

$$h_\alpha = \frac{\delta F}{\delta p_\alpha} = \frac{\partial f}{\partial p_\alpha} - \partial_\beta \frac{\partial f}{\partial (\partial_\beta p_\alpha)}. \quad (3)$$

Taking the variation of the free energy, we have

$$\delta F = \int_V (-\mathbf{h}) \cdot \delta \mathbf{p} d\mathbf{x}. \quad (4)$$

The variation of \mathbf{p} is calculated by

$$\delta \mathbf{p} = \frac{\partial \mathbf{p}}{\partial t} \delta t = [-\mathbf{v} \cdot \nabla \mathbf{p} - \mathbf{\Omega} \cdot \mathbf{p} + \nu \mathbf{D} \cdot \mathbf{p}] \delta t, \quad (5)$$

which is the virtual variation of \mathbf{p} . A virtual deformation is assumed to take place in a very short period of time, so that the other quantities in the transport equation for \mathbf{p} are higher order effects relative to the virtual deformation. We substitute $\delta \mathbf{p}$ in the above variation and obtain

$$\begin{aligned} \delta F &= \int_V (-\mathbf{h}) \cdot [-\mathbf{v} \cdot \nabla \mathbf{p} - \mathbf{\Omega} \cdot \mathbf{p} + \nu \mathbf{D} \cdot \mathbf{p}] \delta t d\mathbf{x} \\ &= \int_V \left[h_\alpha v_\beta \partial_\beta p_\alpha + \frac{1}{2} \partial_\beta v_\alpha (p_\alpha h_\beta - h_\alpha p_\beta) \right. \\ &\quad \left. - \frac{\nu}{2} \partial_\beta v_\alpha (p_\alpha h_\beta + h_\alpha p_\beta) \right] \delta t d\mathbf{x}. \end{aligned} \quad (6)$$

The change in free energy is due to the work done to the system internally

$$\delta F = \int_V [\partial_\beta v_\alpha \sigma_{\alpha\beta}^r - v_\beta F_\beta^{(e)}] d\mathbf{x} \delta t, \quad (7)$$

where σ^r is the reactive stress and $F^{(e)}$ is the elastic force, which are identified as follows:

$$\sigma^r = -\frac{v}{2}(\mathbf{p}\mathbf{h} + \mathbf{h}\mathbf{p}) + \frac{1}{2}(\mathbf{p}\mathbf{h} - \mathbf{h}\mathbf{p}), \quad F_\beta^{(e)} = -h_\alpha \partial_\beta p_\alpha. \quad (8)$$

Notice that

$$\begin{aligned} F_\beta^{(e)} &= -h_\alpha \partial_\beta p_\alpha \\ &= \left[\frac{\partial f}{\partial p_\alpha} - \partial_\gamma \frac{\partial f}{\partial (\partial_\gamma p_\alpha)} \right] \partial_\beta p_\alpha \\ &= -\partial_\gamma \left(\frac{\partial f}{\partial (\partial_\gamma p_\alpha)} \partial_\beta p_\alpha \right) + \partial_\beta f. \end{aligned} \quad (9)$$

Hence, we identify the Ericksen stress tensor as

$$\sigma_{\beta\gamma}^e = f \delta_{\beta\gamma} - \frac{\partial f}{\partial (\partial_\gamma p_\alpha)} \partial_\beta p_\alpha. \quad (10)$$

This is the stress yielded by the elastic external force due to the molecular convection. Denote $(\nabla \mathbf{p})_{\alpha\beta} = \partial_\alpha p_\beta$ and $\tau_{\alpha\beta} = \partial f / [\partial (\partial_\beta p_\alpha)]$, then $\sigma^e = f\mathbf{I} - (\nabla \mathbf{p}) \cdot \tau$. We remark that in the active liquid crystal model presented in Refs. [46] and [47], the Ericksen stress was not considered. Therefore, we emphasize the importance of a systematic derivation of the transport equations for the complex fluid system to ensure the accuracy, consistency and completeness of the hydrodynamic quantities.

In this model, we specify the free energy for the active liquid crystal system as follows:

$$F = \int_V d\mathbf{r} \left[\frac{K_1}{2} (\nabla \cdot \mathbf{p})^2 + \frac{K_3}{2} (\nabla \times \mathbf{p})^2 - \frac{h_1}{2} \|\mathbf{p}\|^2 + \frac{h_2}{4} \|\mathbf{p}\|^4 \right], \quad (11)$$

where $K_{1,3}$ are the splay and bend elastic constants.^[20,54] The last two terms on the right hand side determine the homogeneous steady state of the system in the absence of the molecular activity, which is also termed the bulk energy. We retain the bulk energy in this model to allow the model to be valid in the liquid crystal defect state where the polarity vector vanishes at the defect core. If we insist on a fixed length in \mathbf{p} , then the energy may have a singularity at the defect core where the orientation of the polarity vector is undefined. Modeling singularity using a vector for liquid crystals has undergone several decades of evolution. A consensus seems to have emerged in that a “variable length” internal variable can better handle the singular situation in dynamical states of the system than one with a “fixed length”. We therefore adopt this formulation by not imposing a constraint on the length of the vector. In addition, we could have inserted another Frank elastic mode into the distortional energy corresponding to K_2 . Since the addition will not alter the important outcomes significantly, we choose to ignore it. The current assumption implies that the bend and twist energy are comparable.

The active stress σ^a , reaction stress σ^r , and viscous stress σ^d are given identically as those derived in Refs. [14], [15], and [54]. The hydrodynamic equations for an incompressible polar active liquid crystal solution are then summarized as follows:

$$\begin{aligned} \frac{\partial \mathbf{p}}{\partial t} + (\mathbf{v} + \omega \mathbf{p}) \cdot \nabla \mathbf{p} + \Omega \cdot \mathbf{p} &= \frac{1}{\gamma} \mathbf{h} + \lambda \Delta \mu \mathbf{p} + \nu \mathbf{D} \cdot \mathbf{p}, \\ \frac{\partial (\rho \mathbf{v})}{\partial t} + \nabla \cdot (\rho \mathbf{v} \mathbf{v}) &= \nabla \cdot \sigma, \quad \nabla \cdot \mathbf{v} = 0, \\ \sigma &= \sigma^r + \sigma^d + \sigma^a + \sigma^e - \Pi \mathbf{I}, \\ \sigma^r &= -\frac{v}{2}(\mathbf{p}\mathbf{h} + \mathbf{h}\mathbf{p}) + \frac{1}{2}(\mathbf{p}\mathbf{h} - \mathbf{h}\mathbf{p}), \quad \sigma^d = 2\eta \mathbf{D}, \\ \sigma^a &= \beta (\nabla \mathbf{p} + \nabla \mathbf{p}^T) + \zeta \Delta \mu \mathbf{p} \mathbf{p}, \\ \sigma^e &= f\mathbf{I} - (\nabla \mathbf{p}) \cdot \tau \\ &= f\mathbf{I} - (\nabla \mathbf{p}) \cdot (K_1 (\nabla \cdot \mathbf{p}) \mathbf{I} - K_3 (\nabla \mathbf{p} - \nabla \mathbf{p}^T)), \\ \nabla \cdot \sigma^e &= -(\nabla \mathbf{p}) \cdot \mathbf{h}, \\ \mathbf{h} &= h_1 \mathbf{p} - h_2 \|\mathbf{p}\|^2 \mathbf{p} + (K_1 - K_3) \nabla (\nabla \cdot \mathbf{p}) + K_3 \nabla^2 \mathbf{p}, \end{aligned} \quad (12)$$

where Π is the hydrostatic pressure, η is the viscosity of the host matrix, β is the generalized active viscosity, whose role will be explored in detail in this paper. The active contributions to the mechanical stress is proportional to $\Delta \mu$ and is characterized by the coefficient ζ , $\zeta \Delta \mu > 0$ corresponds to a contractile force couple generated by the active molecule/particle in swimmers, the ALC system is known as the puller; $\zeta \Delta \mu < 0$ corresponds to an extensile force couple on the active particle, which is known as the pusher case. Taking into account the transport equation of \mathbf{p} , we rewrite the reactive stress in an alternative form

$$\begin{aligned} \sigma^r &= \frac{1-v}{2} \gamma \dot{\mathbf{p}} \mathbf{p} - \frac{1+v}{2} \gamma \mathbf{p} \dot{\mathbf{p}} - \frac{1-v}{2} \nu \gamma \mathbf{p} \mathbf{p} \cdot \mathbf{D} \\ &\quad + \frac{1+v}{2} \nu \gamma \mathbf{D} \cdot \mathbf{p} \mathbf{p} + \frac{1-v}{2} \gamma \omega \mathbf{p} \mathbf{p} \cdot \nabla \mathbf{p} \\ &\quad - \frac{1+v}{2} \gamma \omega \mathbf{p} \cdot \nabla \mathbf{p} \mathbf{p} + \gamma \lambda \nu \Delta \mu \mathbf{p} \mathbf{p}. \end{aligned} \quad (13)$$

As a result, in the reactive stress, an active term $\gamma \lambda \nu \Delta \mu \mathbf{p} \mathbf{p}$ is identified. The total activity parameter can be effectively identified as $\zeta + \gamma \lambda \nu$. Analogously, another anisotropic, active component in the reactive stress can be identified as

$$\frac{1-v}{2} \gamma \omega \mathbf{p} \mathbf{p} \cdot \nabla \mathbf{p} - \frac{1+v}{2} \gamma \omega \mathbf{p} \cdot \nabla \mathbf{p} \mathbf{p},$$

which yields an asymmetric tensor due to self-propulsion.

2.2. Energy dissipation

The time derivative of the total energy $F^{\text{tol}} = \int_V (\rho \|\mathbf{v}\|^2 / 2 + f) d\mathbf{x}$ of the material system in a fixed material volume V is given by

$$\frac{dF^{\text{tol}}}{dt} = \int_V d\mathbf{x} \left\{ \partial_t \left(\frac{1}{2} \rho v^2 \right) + \partial_t f(\mathbf{p}, \nabla \mathbf{p}) \right\}. \quad (14)$$

Using the conservation law of mass and momentum as well as the free energy variation of \mathbf{p} and following the divergence

theorem, we obtain

$$\begin{aligned} \frac{dF^{\text{tol}}}{dt} &= \int_V dx \left\{ \mathbf{v} \cdot (\nabla \cdot (\boldsymbol{\sigma} - \boldsymbol{\sigma}^r - \boldsymbol{\sigma}^e)) \right. \\ &\quad \left. - \mathbf{h} \cdot \left[-\omega \mathbf{p} \cdot \nabla \mathbf{p} + \frac{\mathbf{h}}{\gamma} + \lambda \Delta \mu \mathbf{p} \right] \right\} \\ &= \int_V dx \left\{ -2\eta \mathbf{D} : \mathbf{D} - \frac{\mathbf{h}^2}{\gamma} \right. \\ &\quad \left. - \mathbf{D} : [\zeta \Delta \mu \mathbf{p} \mathbf{p} + \beta (\nabla \mathbf{p} + \nabla \mathbf{p}^T)] \right. \\ &\quad \left. - \mathbf{h} \cdot [-\omega \mathbf{p} \cdot \nabla \mathbf{p} + \lambda \Delta \mu \mathbf{p}] \right\}. \end{aligned} \quad (15)$$

The first and second terms are dissipative. The third, fourth, and fifth terms are active terms, they can increase or decrease the time rate of change of the total energy so that the material system is no longer conservative or dissipative. The appearance of the term $\mathbf{h} \cdot \omega \mathbf{p} \cdot \nabla \mathbf{p}$ is due to the neglect of the momentum of active particles because the mass of the particles is very small and their contribution to the total momentum can be neglected. The third term represents the rate of energy change due to the active stress. The last term measures the rate of energy change due to the self-propelled molecular convection and “active acceleration”.

2.3. Nondimensionalization

The polarity vector \mathbf{p} is dimensionless and is used in this model to measure the strength and direction of polarity and defects. We use a characteristic time scale t_0 , length scale l_0 , mass density scale $\rho_0 = \rho$, and dimensionless scale p_L to non-dimensionalize or scale the physical variables

$$\tilde{t} = \frac{t}{t_0}, \quad \tilde{x} = \frac{x}{l_0}, \quad \tilde{\mathbf{v}} = \frac{\mathbf{v} t_0}{l_0}, \quad \tilde{\Pi} = \frac{\Pi t_0^2}{\rho_0 l_0^2}, \quad \tilde{\mathbf{h}} = \frac{\mathbf{h} t_0^2 p_L}{\rho_0 l_0^2}, \quad \tilde{\mathbf{p}} = \frac{\mathbf{p}}{p_L}.$$

As a result, the following dimensionless parameters are obtained:

$$\begin{aligned} \tilde{\omega} &= \frac{t_0 p_L}{l_0} \omega, \quad \tilde{\gamma} = \frac{t_0 p_L^2}{\rho_0 l_0^2} \gamma, \quad \tilde{\lambda} = t_0 \lambda \Delta \mu, \quad \tilde{\mathbf{v}} = \mathbf{v}, \quad \tilde{h}_1 = \frac{t_0^2 p_L^2}{\rho_0 l_0^2} h_1, \\ \tilde{h}_2 &= \frac{t_0^2 p_L^4}{\rho_0 l_0^2} h_2, \quad \tilde{K}_1 = \frac{t_0^2 p_L^2}{\rho_0 l_0^4} K_1, \quad \tilde{K}_3 = \frac{t_0^2 p_L^2}{\rho_0 l_0^4} K_3, \\ \frac{1}{\tilde{\eta}} &= Re = \frac{\rho_0 l_0^2}{\eta t_0}, \quad \tilde{\beta} = \frac{t_0^2 p_L}{\rho_0 l_0^3} \beta, \quad \tilde{\zeta} = \frac{t_0^2 p_L^2 \Delta \mu}{\rho_0 l_0^2} \zeta, \end{aligned}$$

where Re is the Reynolds number for the fluid matrix, and K_i are proportional to the reciprocal of the Ericksen number. Depending on parameter λ , there can exist two states: the isotropic and liquid crystal states. If $\gamma \lambda \Delta \mu + h_1 \leq 0$, we choose the dimensionless scaling parameter $p_L = 1$, the system has a stable isotropic solution $\tilde{\mathbf{p}} = \mathbf{0}$, $\tilde{\mathbf{v}} = \mathbf{0}$. However, if $\gamma \lambda \Delta \mu + h_1 > 0$, then we can choose an appropriate p_L such that $p_L^2 = (\gamma \lambda \Delta \mu + h_1)/h_2$ to ensure $\tilde{\gamma} \tilde{\lambda} + \tilde{h}_1 = \tilde{h}_2$ in the dimensionless form. Then, there is a constant liquid crystal state $\tilde{\mathbf{p}} = \tilde{\mathbf{p}}_0$, $\tilde{\mathbf{v}} = \mathbf{0}$ with $\|\tilde{\mathbf{p}}_0\| = 1$. For simplicity, we drop the \sim on the dimensionless variables and the parameters. The system of governing equations for the active liquid crystal model in

these dimensionless variables are then given by

$$\begin{aligned} \frac{\partial \mathbf{p}}{\partial t} &+ (\mathbf{v} + \omega \mathbf{p}) \cdot \nabla \mathbf{p} + \Omega \cdot \mathbf{p} = \frac{1}{\gamma} \mathbf{h} + \lambda \mathbf{p} + \mathbf{v} \mathbf{D} \cdot \mathbf{p}, \\ \frac{\partial \mathbf{v}}{\partial t} &+ \nabla \cdot (\mathbf{v} \mathbf{v}) = \nabla \cdot \boldsymbol{\sigma}, \quad \nabla \cdot \mathbf{v} = 0, \\ \boldsymbol{\sigma} &= -\Pi \mathbf{I} + \boldsymbol{\sigma}^e + 2\eta \mathbf{D} + \beta (\nabla \mathbf{p} + \nabla \mathbf{p}^T) + \zeta \mathbf{p} \mathbf{p} \\ &\quad - \frac{\mathbf{v}}{2} (\mathbf{p} \mathbf{h} + \mathbf{h} \mathbf{p}) + \frac{1}{2} (\mathbf{p} \mathbf{h} - \mathbf{h} \mathbf{p}), \\ \nabla \cdot \boldsymbol{\sigma}^e &= -(\nabla \mathbf{p}) \cdot \mathbf{h}, \\ \mathbf{h} &= h_1 \mathbf{p} - h_2 \|\mathbf{p}\|^2 \mathbf{p} + (K_1 - K_3) \nabla (\nabla \cdot \mathbf{p}) + K_3 \nabla^2 \mathbf{p}. \end{aligned} \quad (16)$$

When $h_1 + \gamma \lambda > 0$, we denote $\tilde{h}_1 = h_1 + \gamma \lambda = h_2$ and $\tilde{\mathbf{h}} = \mathbf{h} + \gamma \lambda \mathbf{p} = \tilde{h}_1 \mathbf{p} - h_2 \|\mathbf{p}\|^2 \mathbf{p} + (K_1 - K_3) \nabla (\nabla \cdot \mathbf{p}) + K_3 \nabla^2 \mathbf{p}$, then

$$\begin{aligned} \mathbf{p} \mathbf{h} - \mathbf{h} \mathbf{p} &= \mathbf{p} \tilde{\mathbf{h}} - \tilde{\mathbf{h}} \mathbf{p}, \quad \mathbf{p} \mathbf{h} + \mathbf{h} \mathbf{p} = \mathbf{p} \tilde{\mathbf{h}} + \tilde{\mathbf{h}} \mathbf{p} - 2\gamma \lambda \mathbf{p} \mathbf{p}, \\ \nabla \cdot \boldsymbol{\sigma}^e &= -(\nabla \mathbf{p}) \cdot \mathbf{h} = -(\nabla \mathbf{p}) \cdot \tilde{\mathbf{h}} + \frac{1}{2} \gamma \lambda \nabla \cdot (\|\mathbf{p}\|^2 \mathbf{I}). \end{aligned} \quad (17)$$

This is equivalent to absorbing the active term $\lambda \gamma \|\mathbf{p}\|^2/2$ into the equilibrium free energy F to create an effective free energy density $f + \lambda \gamma \|\mathbf{p}\|^2/2$. We note that the activity parameter λ gives two contributions to the stress, one is the active stress part $\gamma \lambda \mathbf{v} \mathbf{p} \mathbf{p}$, which can be absorbed into the term $\zeta \mathbf{p} \mathbf{p}$, the other is the pressure term $\gamma \lambda \nabla \cdot (\|\mathbf{p}\|^2 \mathbf{I})/2$, which can be absorbed into the pressure term $-\Pi \mathbf{I}$. Let $\tilde{\zeta} = \zeta + \gamma \lambda \mathbf{v}$, $\tilde{\Pi} = \Pi - \gamma \lambda \|\mathbf{p}\|^2/2$, then we can effectively eliminate parameter λ if we use $\tilde{h}_1, \tilde{\mathbf{h}}, \tilde{\zeta}, \tilde{\Pi}$ instead of $h_1, \mathbf{h}, \zeta, \Pi$. So we can further assume $\lambda = 0$ and $h_1 = h_2$ whenever $h_1 + \gamma \lambda > 0$ in the model. However, when we study the isotropic state we use $p_L = 1$ and do not enforce $h_1 = h_2$. We will make this subtle point clear wherever necessary throughout the paper.

We will next study linear stability of the hydrodynamic equilibria and then explore dynamics in a couple of limiting regimes of the hydrodynamical theory. In the context of hydrodynamics, we term this near (hydrodynamic) equilibrium dynamics of the governing system of equations. At the microscopic scale, the ALC system never reaches microscopic equilibrium. At the macroscopic level, however, a hydrodynamic equilibrium is possible under certain conditions. The following section is dedicated to studying the macroscopic dynamics in the neighborhood of these equilibria, with an emphasis on mechanisms for instabilities.

3. Near equilibrium dynamics — linear stability analysis

In this section, we set $p_L = 1$, so that we can study both the isotropic steady state and the liquid crystal state within the same dimensionless system. We note that the governing system of equations admits a constant solution $\mathbf{p}_0 \equiv \mathbf{0}$, $\mathbf{v} \equiv \mathbf{v}_0$, $\Pi \equiv \Pi_0$, where \mathbf{v}_0 is a constant vector, Π_0 is a constant pressure (scalar). In addition, if $\tilde{h}_1 > 0$, $\tilde{h}_1 - h_2 \|\mathbf{p}\|^2 = 0$ leads to another family of constant solutions: $\mathbf{p} \equiv \mathbf{p}_0$, $\mathbf{v} \equiv \mathbf{v}_0$, $\Pi \equiv$

Π_0 , where \mathbf{v}_0 and \mathbf{p}_0 are constant vectors, $\|\mathbf{p}_0\|^2 = \bar{h}_1/h_2$. The first family is identified as the isotropic state and the second is a liquid crystal state. In this section, we study linearized stability of these two families of solutions to describe near equilibrium dynamics in the active material system. We note that $p_0 = \sqrt{\bar{h}_1/h_2}$ defines a local minimum of the effective bulk free energy

$$-\frac{\bar{h}_1}{2}\|\mathbf{p}\|^2 + \frac{h_2}{4}\|\mathbf{p}\|^4,$$

whereas $\mathbf{p}_0 = \mathbf{0}$ corresponds to the local maximum of the bulk free energy potential if $\bar{h}_1 > 0$ and a local minimum when $\bar{h}_1 < 0$. In the limit of zero active stress, the isotropic state is deemed to be thermodynamically unstable when $\bar{h}_1 > 0$ and stable when $\bar{h}_1 < 0$ in the model. For active liquid crystals of our interest here, we will see how the activity of the active liquid crystal coupled to hydrodynamics may affect the stability of both steady states.

3.1. Stability of liquid crystal states

We consider the liquid crystal state given by $\|\mathbf{p}_0\|^2 = \bar{h}_1/h_2$ firstly when $\bar{h}_1 > 0$. We seek the solution of the governing system of equations as follows:

$$\mathbf{v} = \mathbf{v}_0 + \varepsilon \mathbf{v}_1, \quad \mathbf{p} = \mathbf{p}_0 + \varepsilon \mathbf{p}_1, \quad \Pi = \Pi_0 + \varepsilon \Pi_1, \quad (18)$$

where $\varepsilon \ll 1$ and the perturbations are defined by

$$\mathbf{v}_1 = e^{\alpha t + i\mathbf{k} \cdot \mathbf{x}} \mathbf{v}_1^{(0)}, \quad \mathbf{p}_1 = e^{\alpha t + i\mathbf{k} \cdot \mathbf{x}} \mathbf{p}_1^{(0)}, \quad \Pi_1 = e^{\alpha t + i\mathbf{k} \cdot \mathbf{x}} \Pi_1^{(0)},$$

where α is a scalar growth rate, $\mathbf{k} = (k_1, k_2, k_3)$ is the wave vector, $\Pi_1^{(0)}$ is a constant scalar, $\mathbf{v}_1^{(0)} = (v_1^{(0)}, v_2^{(0)}, v_3^{(0)})$, and $\mathbf{p}_1^{(0)} = (p_1^{(0)}, p_2^{(0)}, p_3^{(0)})$ are constant unknown vectors. Truncating at the linear order of ε , we write the governing system of equations for the perturbations into a matrix form

$$\left(\begin{pmatrix} 0 & 0 & 0 \\ 0 & \alpha \mathbf{I} & 0 \\ 0 & 0 & \alpha \mathbf{I} \end{pmatrix} + \begin{pmatrix} 0 & 0 & \mathbf{k} \\ 0 & A & B \\ i\mathbf{k}^T & C & D \end{pmatrix} \right) \begin{pmatrix} \Pi_1^{(0)} \\ \mathbf{p}_1^{(0)} \\ \mathbf{v}_1^{(0)} \end{pmatrix} = 0, \quad (19)$$

where the coefficient matrix is 7×7 , the specific components of the matrix are given in the Appendix A. For zero wave vector $\mathbf{k} = \mathbf{0}$, the matrix components $B = C = D = \mathbf{0}$, $A = 2h_2\mathbf{p}_0\mathbf{p}_0/\gamma$, the problem reduces to $(\alpha\mathbf{I} + A)\mathbf{p}_1^{(0)} = \mathbf{0}$. The growth rates (eigenvalues of A) are all non-positive. However, for the nonzero wave number vector $\mathbf{k} \neq \mathbf{0}$, this linear system can be reduced to a 5×5 system. For example, if $k_1 \neq 0$,

$$v_1^{(0)} = -\frac{k_2}{k_1}v_2^{(0)} - \frac{k_3}{k_1}v_3^{(0)}$$

is obtained from $\mathbf{k} \cdot \mathbf{v}_1^{(0)} = 0$. The linearized momentum equation yields

$$\begin{aligned} \Pi_1^{(0)} &= \frac{1}{ik_1} \left[\alpha \left(\frac{k_2}{k_1}v_2^{(0)} + \frac{k_3}{k_1}v_3^{(0)} \right) - C_{1j}p_j^{(0)} \right. \\ &\quad \left. + D_{11} \left(\frac{k_2}{k_1}v_2^{(0)} + \frac{k_3}{k_1}v_3^{(0)} \right) - D_{12}v_2^{(0)} - D_{13}v_3^{(0)} \right]. \end{aligned}$$

We substitute $\Pi_1^{(0)}$ into the second and third components in the momentum equation to arrive at a 5×5 system for $\mathbf{p}_1^{(0)}$ and v_2, v_3

$$\left(\begin{pmatrix} \alpha & 0 & 0 & 0 & 0 \\ 0 & \alpha & 0 & 0 & 0 \\ 0 & 0 & \alpha & 0 & 0 \\ 0 & 0 & 0 & \alpha & 0 \\ 0 & 0 & 0 & 0 & \alpha \end{pmatrix} + \begin{pmatrix} A_{11} & A_{12} & A_{13} & B'_{12} & B'_{13} \\ A_{21} & A_{22} & A_{23} & B'_{22} & B'_{23} \\ A_{31} & A_{32} & A_{33} & B'_{32} & B'_{33} \\ C'_{21} & C'_{22} & C'_{23} & D'_{22} & D'_{23} \\ C'_{31} & C'_{32} & C'_{33} & D'_{32} & D'_{33} \end{pmatrix} \right) \begin{pmatrix} p_1^{(0)} \\ p_2^{(0)} \\ p_3^{(0)} \\ v_2^{(0)} \\ v_3^{(0)} \end{pmatrix} = 0, \quad (20)$$

where B' , C' , and D' can easily be obtained from B , C , and D

$$B'_{i,j} = B_{i,j} - \frac{k_j}{k_1}B_{i1}, \quad (i = 1, 2, 3; \quad j = 2, 3),$$

$$C'_{i,j} = C_{i,j} - \frac{k_i}{k_1}C_{1j}, \quad (i = 2, 3; \quad j = 1, 2, 3),$$

$$D'_{i,j} = D_{i,j} + (\alpha + D_{11})\frac{k_i k_j}{k_1^2} - \frac{k_i}{k_1}D_{1j}, \quad (i = 2, 3; \quad j = 2, 3).$$

This shows that there are five independent eigen-modes. Since a closed-form expression of the growth rate α is not available in general, we seek special solutions of the eigenvalue problem with respect to selected wave vectors. Without loss of generality, we set $\mathbf{v}_0 = \mathbf{0}$ and $\mathbf{p}_0 = (p, 0, 0)$, where $p = \sqrt{\bar{h}_1/h_2}$. We remark that when we choose the wave vector with $k_1 = 0$, but $k_2 \neq 0$ or $k_3 \neq 0$, we can derive an analogous 5×5 system for \mathbf{p} and two velocity components, which can then be used to study linearized stability for those wave vectors.

3.1.1. Perturbations with Fourier modes varying in $\mathbf{k} = (\mathbf{k}_1, \mathbf{0}, \mathbf{0})$

In this special case, the eigenvalues (or growth rates) are obtained as follows:

$$\begin{aligned} \alpha_1 &= -\frac{K_1}{\gamma}k_1^2 - i\omega p k_1 - \frac{2h_2}{\gamma}p^2, \\ \alpha_{2,3} &= -\frac{1}{2\gamma} \left\{ (K_3 + \eta\gamma)k_1^2 + i\omega\gamma p k_1 \right. \\ &\quad \left. + k_1 \sqrt{((K_3 - \eta\gamma)k_1 + i\omega\gamma p)^2 + A_1} \right\}, \\ \alpha_{4,5} &= -\frac{1}{2\gamma} \left\{ (K_3 + \eta\gamma)k_1^2 + i\omega\gamma p k_1 \right. \\ &\quad \left. - k_1 \sqrt{((K_3 - \eta\gamma)k_1 + i\omega\gamma p)^2 + A_1} \right\}, \end{aligned} \quad (21)$$

where $\bar{\zeta} = \zeta + \nu\lambda\gamma$ is the total activity and

$$A_1 = -K_3(\nu+1)^2\gamma^2 p^2 k_1^2 - 2i\beta(\nu+1)\gamma^2 p - 2\bar{\zeta}(\nu+1)\gamma^2 p^2. \quad (22)$$

Clearly, $\text{Re}(\alpha_1) < 0$. If $A_1 = 0$, the eigenvalues are

$$\alpha_{2,3} = -\frac{K_3}{\gamma}k_1^2 - i\omega p k_1, \quad \alpha_{4,5} = -\eta k_1^2. \quad (23)$$

The five modes are all stable if $A_1 = 0$, which can only occur for a passive liquid crystal system with $K_3 = 0$. For $A_1 \neq 0$, there may be unstable modes. Let us first examine the simplified case where $\omega = \beta = 0$. If $\bar{\zeta}(\nu+1) < 0$, then $A_1 > 0$

for

$$k_1^2 < -\frac{2\bar{\zeta}}{K_3(\nu+1)}.$$

Thus, we have $\alpha_{4,5} > 0$ for

$$0 < k_1 < \frac{-2\bar{\zeta}(\nu+1)}{K_3(\nu+1)^2 + 4K_3\eta\gamma},$$

and $\alpha_{2,3} > 0$ for

$$\frac{2\bar{\zeta}(\nu+1)}{K_3(\nu+1)^2 + 4K_3\eta\gamma} < k_1 < 0,$$

leading to two unstable modes. The range of unstable wave numbers depends on the active parameters, the shape of the active molecules/particles, and the distortional elasticity. The distortional elasticity can reduce the range of unstable wave numbers while the active parameter $\bar{\zeta}$ can enlarge it. However, the modes are stable if $\bar{\zeta}(\nu+1) > 0$; that is, $A_1 < 0$. Hence, the instability condition (26) with respect to the parameters in the limiting case is

$$\bar{\zeta}(\nu+1) < 0. \quad (24)$$

For the general case, the eigenvalues $\alpha_{2,3}$ and $\alpha_{4,5}$ can be rewritten into

$$\begin{aligned} \alpha_{2,3} &= -a(bx^2 + iex + x\sqrt{cx^2 + ifx + d}), \\ \alpha_{4,5} &= -a(bx^2 + iex - x\sqrt{cx^2 + ifx + d}), \end{aligned}$$

where $x = k_1$, a, b, c, d, e, f are real numbers

$$\begin{aligned} a &= \frac{1}{2\gamma}, \quad b = K_3 + \eta\gamma, \quad e = \omega\gamma p, \\ c &= (K_3 - \eta\gamma)^2 - (\nu+1)^2 K_3 \gamma^2 p^2, \\ d &= -2\bar{\zeta}(\nu+1)\gamma^2 p^2 - \omega^2 \gamma^2 p^2, \\ f &= -2\beta(\nu+1)\gamma^2 p + 2\omega(K_3 - \eta\gamma)\gamma p. \end{aligned} \quad (25)$$

We note that $a > 0$, and $b > 0$. The real part of the eigenvalues is positive if

$$\left(\frac{\beta\gamma(\nu+1) - \omega(K_3 - \eta\gamma)}{K_3 + \eta\gamma} \right)^2 > \omega^2 + 2\bar{\zeta}(\nu+1). \quad (26)$$

Thus, the real part of $\alpha_{2,3}$ is positive when

$$-\sqrt{\frac{d + \frac{f^2}{4b^2}}{b^2 - c}} < k_1 < 0,$$

while the real part of $\alpha_{4,5}$ is positive when

$$\sqrt{\frac{d + \frac{f^2}{4b^2}}{b^2 - c}} > k_1 > 0.$$

This analysis indicates that there exist a pair of unstable modes for long to intermediate waves with small to medium $|k_1|$, although the system is stable for short waves ($|k_1| \gg 1$).

We note that ν is a geometric parameter of the active liquid crystal particle. $\nu > 0$ indicates the LC molecule is of a rod

shape and $\nu < 0$ represents a discotic shaped particle. Moreover, if the system consists of passive rods, then the rod tumbles when $0 < \nu < 1$ and aligns when $\nu > 1$ in shear flows. Analogously, the disk tumbles when $-1 < \nu < 0$ and aligns when $\nu < -1$ in simple shear flows.

If the active liquid crystal molecule is a rod ($\nu > 0$) or discotic with $-1 < \nu < 0$, so $\nu+1 > 0$, then the steady state is stable if $\bar{\zeta} > 0$ and unstable if $\bar{\zeta} < 0$.^[20] Hence, the puller system is stable, whereas the pusher system is unstable. On the other hand, if the liquid crystal molecule is a discotic aligner, that is, $\nu+1 < 0$, then the puller is unstable while the pusher is stable. This shows that the geometric feature of the liquid crystal molecule coupled with a self-propelled motion can impact on linear stability of the steady state, which is a new feature of the active liquid crystal system. This instability is the genesis for the active liquid crystal system to have a spontaneous flow, even without a driven flow field. In this sense, equation (26) actually gives a criterion for the formation of spontaneous flow due to molecular activities in the bulk without boundaries or with a periodic boundary condition.

Next, we look closely at a limiting case where $\beta = 0$ while ω may be nonzero to provide some analytical insights. The instability condition (26) for the steady state in the limit reduces to

$$\frac{2\omega^2 K_3 \eta \gamma}{(K_3 + \eta \gamma)^2} + \bar{\zeta}(\nu+1) < 0. \quad (27)$$

If $\nu+1 > 0$ for the rod and the discotic tumbler, then the steady state is unstable only if

$$\bar{\zeta} < -\frac{2\omega^2 K_3 \eta \gamma}{(\nu+1)(K_3 + \eta \gamma)^2} < 0,$$

and completely stable otherwise, indicating that the unstable ALC must be a pusher with a sufficiently small activity. If $\nu+1 < 0$, the instability may occur, provided

$$\bar{\zeta} > -\frac{2\omega^2 K_3 \eta \gamma}{(\nu+1)(K_3 + \eta \gamma)^2} > 0,$$

indicating that the unstable ALC must be a puller with a sufficiently large activity

$$\bar{\zeta}_c = -\frac{2\omega^2 K_3 \eta \gamma}{(\nu+1)(K_3 + \eta \gamma)^2}$$

defines the critical active parameter for the onset of instability, where $\bar{\zeta}(\nu+1)$ scales with ω^2 . The stable versus the unstable region in parameter space $(\nu, \bar{\zeta})$ is shown in Fig. 1, where the curves are separating the stable from the unstable regions (separatrices) are hyperbolas. The size of the unstable regions in the parameter space is in general reduced by the presence of nonzero ω .

Then, we examine another limiting case where $\omega = 0, \beta \neq 0$. The instability condition (26) for this case is given

by

$$\left(\frac{\beta\gamma(v+1)}{K_3+\eta\gamma}\right)^2 > 2\bar{\zeta}(v+1). \quad (28)$$

If $(v+1) > 0$, then the steady state is unstable when

$$\bar{\zeta} < \bar{\zeta}_c = \frac{(v+1)(\beta\gamma)^2}{2(K_3+\eta\gamma)^2},$$

where $\bar{\zeta}_c > 0$, indicating that the active matter system is unstable for pushers and for pullers with a sufficiently small activity. On the other hand, if $(v+1) < 0$, then the steady state is unstable when $\bar{\zeta} > \bar{\zeta}_c$ where $\bar{\zeta}_c < 0$, showing that the system is unstable for pullers and pushers with a sufficiently large activity. Figure 1 depicts the stable versus the unstable regions in the parameter space $(v, \bar{\zeta})$, where the separatrix is a line separating the stable from the unstable region in the parameter space. In both limiting cases, the stability condition depends only on $|\omega|$ and $|\beta|$. The size of the unstable regions is in general enlarged by the presence of a nonzero active viscosity.

Finally, we consider the general case ($\beta \neq 0, \omega \neq 0$). We define $K_3/\eta\gamma = \varepsilon \ll 1$. The instability condition (26) can be rewritten as

$$\left(\frac{\beta_r(v+1)+1-\varepsilon}{1+\varepsilon}\right)^2 - 1 = \frac{(\beta_r(v+1)-2\varepsilon)(\beta_r(v+1)+2)}{(1+\varepsilon)^2} > 2\zeta_r(v+1), \quad (29)$$

where $\beta_r = \beta/\omega\eta$, $\zeta_r = \bar{\zeta}/\omega^2$. Because the ratio β/ω is the additional viscosity due to the self-motion of the active particles, the new parameter β_r can be considered as the active viscosity relative to the viscosity of the surrounding fluid. The new parameter ζ_r can be considered as the strength of activity relative to self-motion of the active particles.

The stable versus unstable regions are summarized in Fig. 1 in the parameter space $(v, \bar{\zeta})$, (v, ζ_r) , and (v, ζ_r, β_r) , respectively. When β and ω are both zero, the stable and unstable regions are separated by two perpendicular straight lines. While $\beta = 0$ and ω may be nonzero, the unstable region shrinks, making the stable region a well-connected region that separates from the unstable regions by a pair of hyperbolas. When $\omega = 0$ while β may be nonzero, the stable region and the unstable region are separated by a line whose slope scales with β^2 and the unstable region is enlarged. Clearly, a nonzero ω is stabilizing while a nonzero β is destabilizing. When both are nonzero and $\beta > 0$, in general, the unstable region shifts upward and shifts downward when $\beta < 0$. More complete results are shown in the space of rescaled parameters (v, ζ_r, β_r) , where the separatrices between the stable and unstable regions are depicted. When projected onto 2D parameter space (v, ζ_r) , the evolution of the separatrices are shown in Fig. 1(b), where the unstable region again shifts downward as β_r decreases. We note that the effect of β is asymmetric in that positive and negative values of β of the same magnitude defines different unstable regions in the parameter space $(v, \bar{\zeta})$ ($\omega \neq 0$) and its role is in general destabilizing.

In order to examine the unstable manifold corresponding to the unstable mode, we calculate the components of the corresponding eigenvectors of the linearized system. We find that the unstable manifold is a 2D subspace embedded in $(p_2^{(0)}, p_3^{(0)}, v_2^{(0)}, v_3^{(0)}) \in \mathbb{C}^4$. These unstable modes clearly couple the orientational dynamics to hydrodynamics in the plane perpendicular to the direction in which the perturbations vary. We next consider perturbations varying in x_2 direction to investigate what instability can occur.

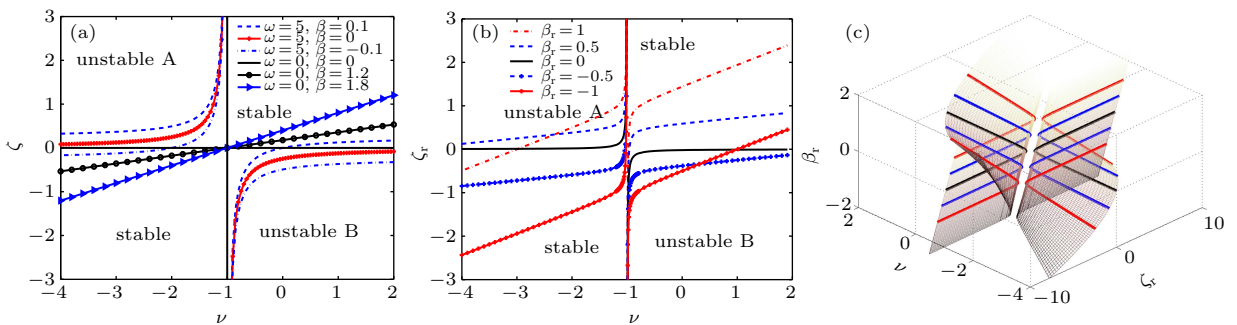


Fig. 1. Diagrams for regions of stability with respect to perturbations varying in $(k_1, 0, 0)$. The parameter values are $K_3 = 0.01, \eta = 2, \gamma = 1$. (a) Stability diagram in $(v, \bar{\zeta})$ space. The black solid lines denote the boundaries between the stable and unstable regions for $\omega = 0, \beta = 0$. The red lines with “+” denote the boundaries between the stable and unstable regions for $\omega \neq 0, \beta = 0$. The blue dashed and dash-dot lines denote the boundaries between the stable and unstable regions for $\omega \neq 0, \beta \neq 0$. (b) Stability diagram in (v, ζ_r) space with $\omega \neq 0$. Boundaries at selected values of $\beta_r = 1, 0.5, 0, -0.5, -1$ are depicted. These curves are shown as contour lines in the 3D boundary surfaces shown in panel (c). (c) Stability diagram in (v, ζ_r, β_r) space with $\omega \neq 0$. Two separatrices (surfaces) in the 3D parameter space are shown.

3.1.2. Perturbations with Fourier modes varying in $k = (0, k_2, 0)$

Here, we examine the perturbation varying in the x_2 direction; that is, $k = (0, k_2, 0)$. We rederive a new 5×5 reduced linearized system for the stability analysis assuming $k_2 \neq 0$.

The eigenvalues of the dispersion equation corresponding to this perturbation are given by

$$\alpha_1 = -\eta k_2^2, \quad \alpha_2 = -\frac{K_3}{\gamma} k_2^2, \quad \alpha_3 = -\frac{K_3}{\gamma} k_2^2 - \frac{2h_2}{\gamma} p^2,$$

$$\alpha_4 = -\frac{1}{2\gamma} \left\{ (K_1 + \eta\gamma)k_2^2 + k_2 \sqrt{(K_1 - \eta\gamma)^2 k_2^2 + A_2} \right\},$$

$$\alpha_5 = -\frac{1}{2\gamma} \left\{ (K_1 + \eta\gamma)k_2^2 - k_2 \sqrt{(K_1 - \eta\gamma)^2 k_2^2 + A_2} \right\}, \quad (30)$$

where $A_2 = 2\bar{\zeta}(1-\nu)\gamma^2 p^2 - K_1(\nu-1)^2 \gamma^2 p^2 k_2^2$. It is easy to find that $\alpha_{1,2,3} < 0$ for $k_2 \neq 0$. If $A_2 = 0$, then we have $\alpha_4 = -K_1 k_2^2 / \gamma$, $\alpha_5 = -\eta k_2^2$. For $A_2 \neq 0$, we denote

$$a = \frac{1}{2\gamma}, \quad b' = K_1 + \eta\gamma, \quad c' = (K_1 - \eta\gamma)^2 - K_1(\nu-1)^2 \gamma^2 p^2,$$

$$d' = 2\bar{\zeta}(1-\nu)\gamma^2 p^2.$$

The eigenvalues α_4 and α_5 can be written as

$$\alpha_4 = -a(b'k_2^2 + k_2 \sqrt{c'k_2^2 + d'}), \quad \alpha_5 = -a(b'k_2^2 - k_2 \sqrt{c'k_2^2 + d'}).$$

Notice that $a > 0, b' > 0$ and $(b')^2 - c' = 4K_1\eta\gamma + K_1(\nu-1)^2 \gamma^2 p^2 > 0$. The eigenvalues α_4 and α_5 can be positive for some wave numbers k_2 only if $d' > 0$, that is

$$\bar{\zeta}(1-\nu) > 0, \quad (31)$$

where eigenvalue α_4 is positive for

$$-\sqrt{\frac{d'}{(b')^2 - c'}} < k_2 < 0,$$

eigenvalue α_5 is positive for

$$\sqrt{\frac{d'}{(b')^2 - c'}} > k_2 > 0.$$

Thus, for any given wave number, there can exist a unique unstable mode. Notice that

$$\frac{d'}{b'^2 - c'} = \frac{2\bar{\zeta}(1-\nu)}{K_1 \left[(\nu-1)^2 + \frac{4\eta}{\gamma p^2} \right]}.$$

The range of the instability is once again affected by $\bar{\zeta}$ and inversely by the distortional elasticity K_1 and viscosity ratio η/γ . This mode of instability is completely independent of the active parameters β and ω , unlike in the type of instability that was discussed previously. Figure 2 shows the phase diagram for this mode of instability. From the eigenvectors corresponding to the positive growth rate, we notice that the 1D unstable manifold sits in the subspace $(\Pi_1^{(0)}, p_2^{(0)}, v_1^{(0)}) \in C^3$. Therefore, the instability is a result of the coupling between the velocity component v_1 , pressure, and the polarity vector component in the direction in which the perturbation varies.

In the case where the perturbation varies only in the x_3 direction, that is, $\mathbf{k} = (0, 0, k_3)$, we find that the eigenvalues are identical to the case of $\mathbf{k} = (0, k_2, 0)$, except that the eigenvector corresponding to the unstable eigenvalue sits in the subspace $(\Pi_1^{(0)}, p_3^{(0)}, v_1^{(0)}) \in C^3$, which generates the 1D unstable manifold. As a matter of fact, the eigenvalue results are identical for all $\mathbf{k} = (0, k_2, k_3)$. In the general case, the eigenvector corresponding to the unstable eigenvalue sits in $(\Pi_1^{(0)}, p_2^{(0)}, p_3^{(0)}, v_1^{(0)}) \in C^4$. The polarity vector component in

the 1D unstable manifold is related to the direction in which the perturbation varies in the (y, z) plane, the pressure and v_1 .

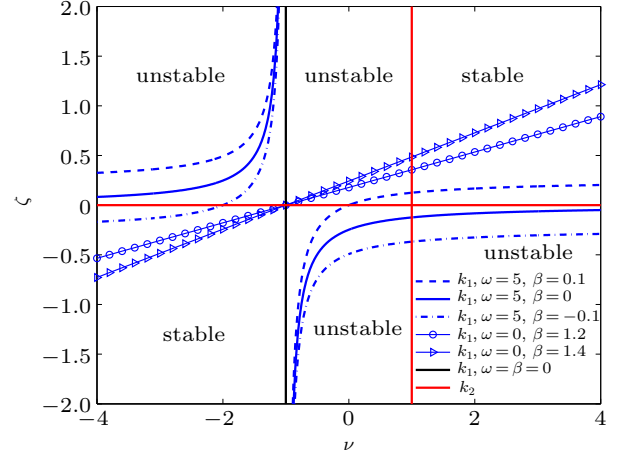


Fig. 2. Stability diagram in $(\nu, \bar{\zeta})$ space for the liquid crystal phase. The parameter values are $K_3 = 0.01, \eta = 2, \gamma = 1$. The red lines are the separatrices for the regions of $\bar{\zeta}(1-\nu) > 0$ and the regions of $\bar{\zeta}(1-\nu) < 0$, separating the stable regions from those of the unstable ones subject to perturbations varying in the x_2 direction. The separatrices between the stable regions and the unstable ones subject to perturbations varying in the x_1 direction are given by the other curves. If $\beta = 0, \omega \neq 0$, then the separatrices are hyperbolic curves. If we fix $\omega = 5$, then increasing $|\beta|$ uplifts the curves when $\beta < 0$ while downshifts the curves when $\beta > 0$, altering the boundaries of the unstable regions. The overall stable regions for the ALC system subject to both types of perturbations are the overlapping stable regions of each mode, which consist of subsets in $\bar{\zeta} < 0, \nu < -1$ and $\bar{\zeta} > 0, \nu > 1$. The ALC systems that are stable to the two perturbations are either discotic pushers or rod pullers. The general trend of β in the model is to reduce the size of the overall stable region.

In summary, long-wave linear instability for the liquid crystal state can emerge in distinct submanifolds of dimensions two and one, respectively, depending on the direction in which the perturbations vary. When the perturbation varies in the direction parallel to the steady liquid crystal phase, there exists a 2D unstable manifold containing the polarity vector component perpendicular to the direction of the steady state liquid crystal state. While the perturbation varies transverse to the steady state, there exists a 1D unstable submanifold containing the polarity vector components parallel to the perturbed wave vector. So the unstable polarity vector component in the submanifold is always perpendicular to the direction of the steady state polarity direction. The stability diagram for the ALC system is depicted in Fig. 2, where the overlaying stability region from both modes indicates the overall system stability; otherwise, there may exist one or two modes of instability leading to potential spontaneous flows. The results show that the stability is only possible when the underlying active liquid crystal is a flow-aligner. Even for a flow-aligner, its stability is determined ultimately by the active parameters $\bar{\zeta}, \beta, \omega$. We comment that the limiting case of this stability diagram at $\beta = \omega = 0$ has been obtained by Edwards and Yeomans for a channel flow using a tensor based ALC model.^[46] With the additional active parameters β and ω the stability region is reduced or enlarged depending on the relative strength

of these two in the first mode of instability. The second mode of instability is independent of the active parameters β and ω .

3.2. Stability of the isotropic state

For isotropic state $p_0 = 0$, the wave vector in the Fourier modes of the perturbations is parameterized by $\mathbf{k} = k(\sin \theta \cos \phi, \sin \theta \sin \phi, \cos \theta)$ in spherical coordinates. The linear growth rates are obtained as follows:

$$\alpha_1 = -\frac{1}{\gamma}(K_1 k^2 - \bar{h}_1), \quad \alpha_{2,3} = -\frac{1}{\gamma}(K_3 k^2 - \bar{h}_1),$$

$$\alpha_{4,5} = -\eta k^2. \quad (32)$$

It is apparent that $\text{Re}(\alpha_{4,5}) < 0$, α_1 is positive when $|k| < \sqrt{\bar{h}_1/K_1}$; α_2, α_3 are positive when $|k| < \sqrt{\bar{h}_1/K_3}$. Therefore, there is the possibility of growth in a three-dimensional manifold for long-waves provided a liquid crystal phase exists; that is, $\bar{h}_1 > 0$. Notice that \bar{h}_1 depends on λ . So long as the active liquid crystal system admits a liquid crystal phase as well as an isotropic phase, the isotropic phase is deemed to be unstable to long-wave perturbations. The range of the unstable wave number is determined by the Frank elastic constants, as well as by the leading coefficient in the effective bulk free energy that determines the liquid crystal phase. From the corresponding eigenvectors, we notice that the three-dimensional unstable manifold associated with the unstable modes sits in the subspace $(\mathbf{p}_1^{(0)}, \mathbf{v}_1^{(0)}) \in C^6$. When $\bar{h}_1 < 0$, the isotropic state is the only stable steady state.

This simple analysis shows that this activity can stabilize the otherwise unstable liquid crystal phase provided that the activity generates a strong enough negative parameter λ . Otherwise, the isotropic steady state is always unstable with respect to long-wave disturbances. However, for most active liquid crystal systems, parameter λ is perceived as positive, so that the instability for the isotropic state persists. The parameter can also be perceived as a controlling parameter for the acceleration of the deceleration of the self-moving molecules. Physically, the stable isotropic state is a possibility, provided that the self-moving molecules decelerate quickly enough.

4. 1D heterogeneous structures in the viscous stress dominated regime

Having studied the stability of constant steady states in an infinite or a periodic domain that can lead to spontaneous flows in the active matter system, we next study solutions of the governing system of equations that are homogeneous in two space dimensions, say (x, z) , while inhomogeneous in the confined third direction, y direction. Specifically, we want to find the solution of the governing equations in the following form:

$\mathbf{p} = (p_1(y, t), p_2(y, t), p_3(y, t))$, $\mathbf{v} = (v_1(y, t), v_2(y, t), v_3(y, t))$, and $\nabla \Pi$ is a function of (y, t) . Because the flow is incompressible, $\nabla \cdot \mathbf{v} = 0$, $\partial v_2 / \partial y = 0$, $v_2 = v_2(t)$. If we impose the

no-slip boundary condition for the velocity field, $v_2 = 0$. We focus on the viscous stress dominated regime of the model in this section, in which the momentum equation is dominated by the viscous stress and pressure, given approximately by

$$\eta \nabla^2 \mathbf{v} = \nabla \Pi. \quad (33)$$

If Π is a constant, a general solution for \mathbf{v} is given by $\mathbf{v} = \mathbf{A} \cdot \mathbf{x}$, where \mathbf{A} is a 3×3 matrix with trace zero due to $\nabla \cdot \mathbf{v} = 0$. One special case of the solution is

$$\mathbf{A} = \begin{pmatrix} 0 & Pe & 0 \\ 0 & 0 & 0 \\ 0 & 0 & 0 \end{pmatrix}, \quad (34)$$

that is, $\mathbf{v}(y, t) = (Pe y, 0, 0)$, $\Pi = \text{const}$, which is known as the simple steady shear flow solution or plane Couette flow solution, where Pe is a constant, known as the shear rate or the Peclet number. There are other linear flow fields that are important and interesting in understanding the hydrodynamics of the flowing active material system. However, we will limit our study to the simple shear flow in linear flows.

If instead $\nabla \Pi$ is a particular constant vector $\nabla \Pi = (-2Pe, 0, 0)$, then we have a special nonlinear solution from the momentum equation

$$\mathbf{v} = (Pe y(1 - y), 0, 0). \quad (35)$$

This steady flow field is called the Poiseuille flow field. In the following, we will focus on investigating response dynamics of the polarity vector with respect to these two types of special flows in the viscous stress dominated regime.

4.1. Steady shear flow

For the simple shear flow: $\mathbf{v}(y, t) = (Pe y, 0, 0)$, the equation for polarity vector \mathbf{p} reduces to

$$\begin{aligned} \frac{\partial p_1}{\partial t} + \omega p_2 \frac{\partial p_1}{\partial y} - \frac{1}{2} Pe(v + 1) p_2 - \frac{1}{\gamma} (h_1 - h_2 \|\mathbf{p}\|^2) p_1 \\ - \lambda p_1 - \frac{K_3}{\gamma} \frac{\partial^2 p_1}{\partial y^2} = 0, \\ \frac{\partial p_2}{\partial t} + \omega p_2 \frac{\partial p_2}{\partial y} + \frac{1}{2} Pe(1 - v) p_1 - \frac{1}{\gamma} (h_1 - h_2 \|\mathbf{p}\|^2) p_2 \\ - \lambda p_2 - \frac{K_1}{\gamma} \frac{\partial^2 p_2}{\partial y^2} = 0, \\ \frac{\partial p_3}{\partial t} + \omega p_2 \frac{\partial p_3}{\partial y} - \frac{1}{\gamma} (h_1 - h_2 \|\mathbf{p}\|^2) p_3 \\ - \lambda p_3 - \frac{K_3}{\gamma} \frac{\partial^2 p_3}{\partial y^2} = 0. \end{aligned} \quad (36)$$

This is a coupled PDE system. The activity is reflected in the growth term $\lambda \mathbf{p}$ only. In most active liquid crystal systems, the distortional elasticity is weak. Therefore, it would be useful to first examine the limiting case where this effect is weak.

4.1.1. Planar dynamics in the weak distortional elastic limit

It is easy to show that $p_3(y, t) = 0$ is a solution of the third equation in Eq. (36). Then, we focus on the solution

of \mathbf{p} confined to the (x, y) plane. We assume that ω , K_1 , and K_3 are all small and neglect the relevant gradient terms to obtain an ODE system of (p_1, p_2) . Using the representation $p_1 = r \cos \theta$, $p_2 = r \sin \theta$ in a polar coordinate, the time-dependent ODE system reduces to

$$r_t = dr - fr^3 - r(b+c) \sin \theta \cos \theta, \quad \theta_t = b \sin^2 \theta - c \cos^2 \theta, \quad (37)$$

where

$$b = -\frac{1}{2}Pe(1+\nu), \quad c = \frac{1}{2}Pe(1-\nu), \quad d = \frac{h_1}{\gamma} + \lambda, \quad f = \frac{h_2}{\gamma}.$$

We discuss the solution of the system in two different cases based on values of the geometric parameter ν .

Case 1 $|\nu| > 1$, the flow-aligning state

In the flow-aligning region $|\nu| > 1$, $bc = a^2(\nu^2 - 1)/4 > 0$, a steady state is possible, which is known as the flow-aligning state or aligner in liquid crystal literature,^[55] where \mathbf{p} aligns with an angle to the flow direction given by

$$\tan \theta = \pm \sqrt{\frac{c}{b}} = \pm \sqrt{\frac{\nu-1}{\nu+1}}. \quad (38)$$

Correspondingly, the amplitude of the steady state is given by the following, if they are valid,

$$r = 0, \quad r = \sqrt{\frac{2d - Pe\nu \sin(2\theta)}{2f}}. \quad (39)$$

Here, $r = 0$ corresponds to the isotropic state and the nonzero r yields a liquid crystal state. This steady liquid crystal state exists only when

$$d - \frac{Pe\nu \sin(2\theta)}{2} > 0,$$

i.e.,

$$d > \frac{Pe\nu \sin(2\theta)}{2}.$$

Notice that d depends on λ linearly. We thus conclude that a steady aligning liquid crystal state exists if $\lambda > 0$ and an isotropic state may exist if $\lambda < 0$ and is sufficient small. The transient solution for the angle can be obtained as follows:

$$\tan \theta = \frac{\sqrt{\frac{c}{b}}(e^{-2ct/\sqrt{c/b}} + 1)}{e^{-2ct/\sqrt{c/b}} - 1}, \quad (40)$$

where $\theta(0) = 0$. When $t \rightarrow \infty$, $\tan \theta \rightarrow \sqrt{c/b}$ ($c < 0$) or $-\sqrt{c/b}$ ($c > 0$), defining the selection criterion for the unique steady state: \mathbf{p} tends to align to the flow direction at a positive angle if $c < 0$ and a negative angle if $c > 0$. The impact of λ is to attain a steady state with a longer polarity vector provided $\lambda > 0$ and shorter one or isotropic steady state with $\lambda < 0$.

Case 2 $|\nu| < 1$, the tumbling state

In the tumbling regime $|\nu| < 1$, $-bc = a(1 - \nu^2)/4 > 0$. Integrating the second equation of Eq. (37)

$$\tan \theta = \sqrt{-c/b} \tan(b\sqrt{-c/b}t), \quad (41)$$

where $\theta(0) = 0$ is used. Then, $\theta(t)$ is an increasing function of t if $b > 0$, decreasing function of t if $b < 0$. The sign of b

is completely determined by the direction of shear. The polarity vector keeps tumbling in time in the active liquid crystal system. Once the angle is determined, the problem for the amplitude of \mathbf{p} reduces to a one-variable ordinary differential equation

$$r_t = dr - fr^3 - r(b+c) \sin \theta \cos \theta, \quad r(0) = p_0. \quad (42)$$

The solution of r is a function of time t . In particular, if $\nu = 0$, then $c = -b$, and we can obtain an analytic solution: $r(t) = \sqrt{d/(f + (d/p_0^2 - f)e^{-2dt})}$, $\theta(t) = bt$. This solution asymptotically approaches a periodic solution given below provided $d > 0$. Additionally, if $d/p_0^2 = f$, then the solution is periodic, where \mathbf{p} rotates in a circle Γ with the center $(0, 0)$, radius $r = \sqrt{d/f}$ and angular speed b . Clearly, this is the time-periodic solution that the spiral solution converges to, even if $d/p_0^2 - f \neq 0$ provided $d > 0$. If $d \leq 0$, that is $\bar{h}_1 \leq 0$, then this solution yields a convergent spiral solution approaching $(0, 0)$ as $t \rightarrow \infty$, indicating that the steady state of the system is the isotropic state. Figure 3 depicts some solutions, including periodic, transient, and steady states. We surmise that $d < 0$ is a condition for the existence of the isotropic steady state in general, which is strongly supported by numerical computations. Notice that $d < 0$ if λ is sufficiently small as a negative number. The solution scenario in general resembles the case of $b + c = 0$ that was qualitatively discussed above.

The dynamics described above are for $p_3 = 0$ in the weak distortional elastic limit. When we allow perturbations in p_3 , we would like to explore if the in-plane solutions can survive.

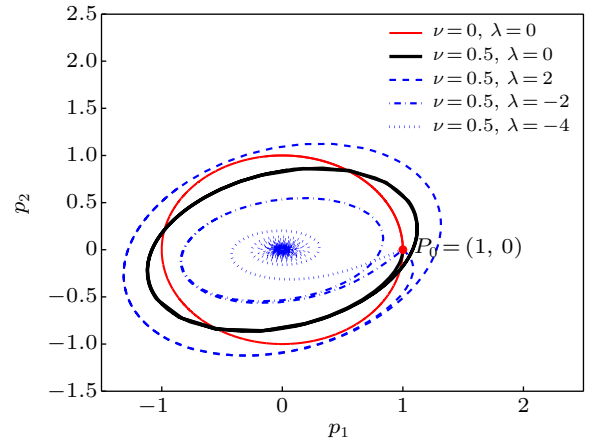


Fig. 3. Orbits of \mathbf{p} in the tumbling region ($|\nu| < 1$). The parameter values are $\gamma = 1, h_1 = h_2 = 4, Pe = 8$. When $\lambda = 0, \nu = 0$, the orbit is a circle, shown in the red curve. The thick black curve depicts the orbit of \mathbf{p} with zero activity ($\lambda = 0, d = f > 0$). The blue dashed curve shows that the positive activity ($\lambda = 2, d > f > 0$) can elongate the length of the polarity vector while the blue dash-dot curve shows that a negative activity ($\lambda = -2, f > d > 0$) can contract the length of the polarity vector. The blue dotted curve shows that if the activity parameter is sufficiently negative ($\lambda = -4, d = 0$), the long time behavior of the polarity vector will contract to the point $(0, 0)$, leading to the isotropic state as the globally stable steady state; for $\lambda < -4, d < 0$, the polarity vector also contracts to the point $(0, 0)$. Thus, λ promotes time periodic attractors if $\lambda > 0$ and in the meantime may arrest the transient states to the unique isotropic state if $\lambda < 0$.

4.1.2. Out-of-plane dynamics in the weak distortional limit

We now allow p_3 to vary in space and time so that the polarity vector can vary in 3D space. We now use spherical coordinate (r, θ, ψ) to parametrize \mathbf{p} . Let $p_1 = r \sin \psi \cos \theta$, $p_2 = r \sin \psi \sin \theta$, $p_3 = r \cos \psi$, the governing equation system becomes

$$\begin{aligned} r_t &= dr - fr^3 - \frac{1}{2}r(b+c)\sin^2 \psi \sin(2\theta), \\ \theta_t &= b \sin^2 \theta - c \cos^2 \theta, \\ \psi_t &= -\frac{1}{4}(b+c)\sin(2\psi)\sin(2\theta). \end{aligned} \quad (43)$$

If $|\nu| > 1$, as discussed above, then the flow-aligning steady state stays in plane, which shows that the solution is stable subject to out-of-plane perturbations. In addition, there exist two more steady states given by $\psi(t) \equiv \psi_0 = 0, \pi$ with $r = 0$ and $r = \sqrt{d/f}$, known as logrolling states. The steady states are liquid crystal states if $d + |Pev|\sqrt{1 - 1/\nu^2} > 0$ and isotropic states otherwise. A linear stability analysis reveals that the only stable steady state is the flow-aligning state. We note that when $d < 0$, the quiescent state admits only an isotropic state. Hence, if there is a stable liquid crystal state when $d + |Pev|\sqrt{1 - 1/\nu^2} > 0$, then it must be induced by the shear flow. If $d < 0$ is small enough, then no liquid crystal phase would be possible unless the shear is large enough such that $d + |Pev|\sqrt{1 - 1/\nu^2} > 0$. This result is unique for active liquid crystal systems.

If $|\nu| < 1$, then $\theta(t)$ is an increasing function with respect to t if $b > 0$, decreasing if $b < 0$. There is no steady solution for $\theta(t)$. If $0 < |\nu| < 1$, then we have $\tan \theta = \sqrt{-c/b} \tan(tb\sqrt{-c/b})$ with $\theta(0) = 0$. We solve the equation of ψ with initial condition $\psi(0) = \psi_0$. The solution is

$$\begin{aligned} \cos(2\psi) &= \frac{(1 + \cos(2\psi)_0)e^{f(t)} - (1 - \cos(2\psi)_0)}{(1 + \cos(2\psi)_0)e^{f(t)} + (1 - \cos(2\psi)_0)}, \\ f(t) &= \int_0^t (b+c)\sin(2\theta)dt. \end{aligned} \quad (44)$$

It is easy to note that $\psi = \psi_0 = 0, \pi/2, \pi$ are steady solutions for ψ , where $\psi = 0, \pi$ yield the logrolling states while $\psi = \pi/2$ corresponds to the in-plane tumbling solution. A simple linear stability analysis shows that the two logrolling states are neutrally stable. Figure 4 depicts some solutions at a set of selected initial values of ψ_0 . These time-dependent solutions show the kayaking behavior. If the director \mathbf{p} is not on (x, y) -plane or is perpendicular to (x, y) -plane in the initial state, then \mathbf{p} rotates continuously around z axis and the elevation angle oscillates in a narrow range, yielding a true kayaking solution. The existence of multiple solutions is the artifact of this model in this particular limit. We will discuss the regularizing mechanism shortly in subsequent sections. However, for $d < 0$, the only stable state the governing system of equation can have is the isotropic state, which is strongly supported by numerical evidence.

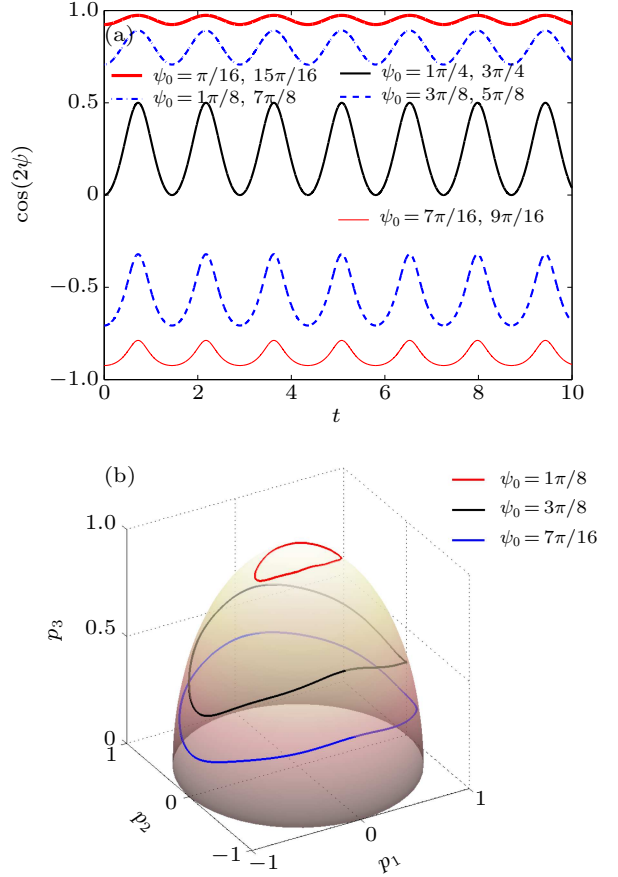


Fig. 4. Kayaking solutions. Here, $Pe = 5, \nu = 0.5$. (a) Time-dependent oscillations of $\cos(2\psi)$ when the initial condition $\psi(0) \neq 0, \pi/2, \pi$. The amplitude is smaller if the initial condition $\psi(0)$ is near the steady states $\psi_0 = 0, \pi/2, \pi$. (b) 3D kayaking orbits of \mathbf{p} with different initial states. The director rotates continuously around z axis under a shear flow. There are infinitely many such kayaking solutions.

We remark that the result for kayaking solutions obtained here is identical with that obtained from the classical Ericksen–Leslie model. Notice that these results are obtained while the distortional elasticity and boundary anchoring condition are ignored. Therefore, these solutions may not survive when the long-range elasticity and the boundary conditions are present in the model.

4.2. Numerical results for spatially inhomogeneous states in shear flow

Having studied the spatially homogeneous states, we next compute the 1D temporal-spatial solutions by considering the effect of distortional elasticity, as well as the boundary condition, numerically. In the following numerical simulations, we focus on the liquid crystal phase so that we set $\lambda = 0$ and $h_1 = h_2$ and the base parameters $K_1 = K_3 = 0.04, h_1 = h_2 = 10, \gamma = 1, \omega = 0, \eta = 1$. The shear rate is set at $Pe = 4$.

Planar dynamics We focus once again on the planar mode first where $p_3 = 0$, and consider the Dirichlet boundary condition (BC) with \mathbf{p} aligned to the wall, the Neumann BC, and the soft anchoring BC, respectively. The theoretical definition of the defect is $\|\mathbf{p}\| = 0$. However, in the numerical

simulations we adopt a numerical one

$$p^d(t) < \varepsilon, \quad (45)$$

where $p^d(t) = \min\{\|\mathbf{p}(y,t)\| : y \in [0,1]\}$ and $\varepsilon = 0.01$.

Figure 5 depicts two representative solutions for the case of bulk or mono-domain tumbling and flow-aligning induced patterns, respectively. In the case of bulk-domain tumbling, a pair of defects are created in space-time periodically in Fig. 5(a) with the Dirichlet BC. Whereas in the flow-aligning case with the Dirichlet BC, the polarity vector only shows a slight tilt away from the anchored orientation due to shear in the interior of the shear cell, where a steady state is reached. Both of these are analogous to what one observes in the study of the passive liquid crystal case.

For the Neumann boundary condition, the polarity vector tumbles uniformly in time and never creates a defective spatial temporal structure, as shown in Fig. 5(c). In the flow-aligning case, the solution approaches a spatially homogeneous flow-aligned state, as shown in Fig. 5(d). Therefore, the mono-domain solution dominates in this case (see Fig. 5). The solution behavior in this boundary condition is essentially the behavior that we observe in the monodomain model that was alluded to in the previous subsection.

In addition to the two extreme boundary anchoring conditions, we explore the soft anchoring boundary condition that interpolates between the Dirichlet and Neumann boundary conditions

$$\frac{\partial \mathbf{p}}{\partial \mathbf{n}} = -\frac{1}{\lambda_b}(\mathbf{p} - \mathbf{p}_0), \quad (46)$$

where λ_b is a positive parameter that measures the strength of anchoring. Here, we firstly consider the tumbling case ($\nu = 0.5$) and focus on the effect of parameter λ_b . The study on soft anchoring boundary conditions at selected values of λ_b shows an evolution from the case of the Dirichlet boundary condition to that of the Neumann boundary condition (see Fig. 6.) There is no defect when anchoring is weak. Defects only start appearing near the boundaries if the strength of the anchoring is strong enough. Figure 6 depicts a sequence of polarity vector solution for tumbling LCs as the strength of anchoring increases from weak to strong. Finally, for the soft anchoring boundary condition, in the flow-aligning region ($|\nu| > 1$), the director \mathbf{p} demonstrates a slight tilt away from the initial state under the shear flow, as we can see in the Dirichlet and Neumann boundary condition cases. These numerical experiments show that the planar mode is dominated by the bulk flow behavior in the interior, even at the presence of boundary anchoring and long-range elastic interaction. When the interior structure has an orientational conflict with the anchoring condition at the walls, a defective structure emerges to mitigate the difference. Otherwise, a slight variation in the orientation structure is necessary to coordinate the orientation at the walls with that in the interior in the flow aligning case. We then lift the constraint on $p_3 = 0$ to investigate how the spatial-temporal structure can change in three-dimensional space.

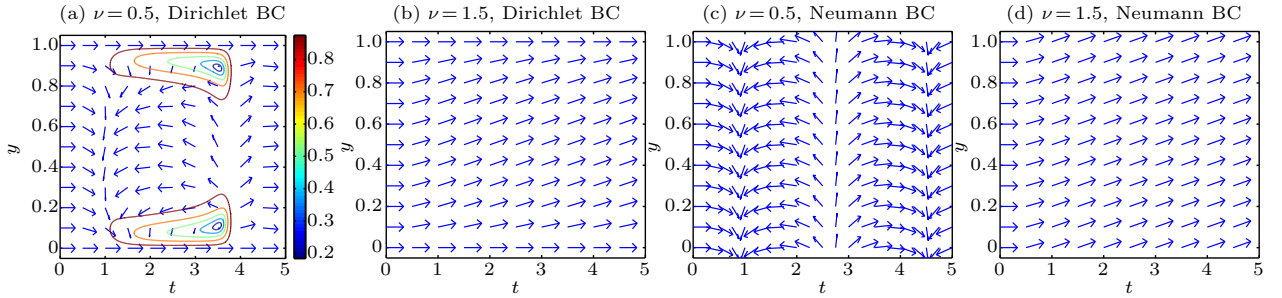


Fig. 5. Planar polarity vector structures with respect to the Dirichlet and Neumann BC, respectively. (a) Tumbling \mathbf{p} with the Dirichlet BC. The contour lines are based on the value of $\|\mathbf{p}\|$. At defects, $\|\mathbf{p}\| \leq \varepsilon$. Two defects show up in the domain near $y = 0.1/0.9$ at $t = 3.5$. (b) Flow-aligning \mathbf{p} with the Dirichlet BC, where \mathbf{p} tends to align to the flow direction at some angle in the steady state in which there is no defect. Panels (c) and (d) show tumbling and aligning structures with the Neumann BC, respectively, where bulk behavior dominates so that there is no defect.

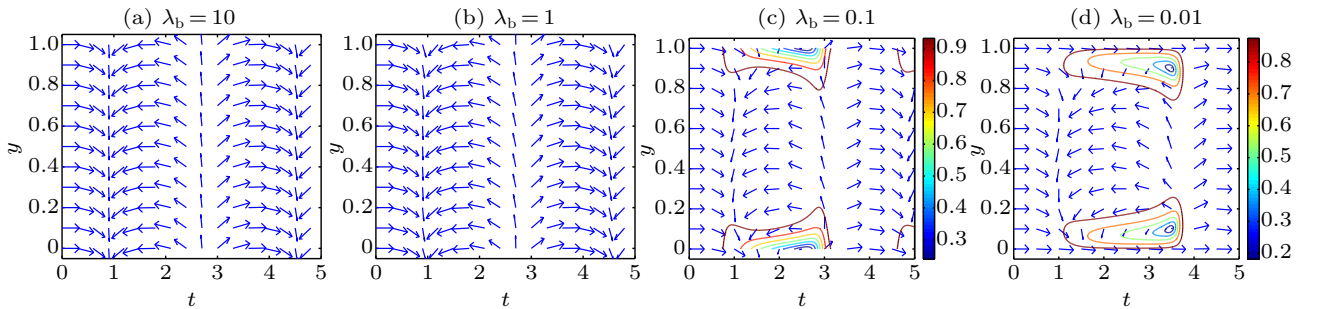


Fig. 6. Evolution of planar polarity vector structures as the strength of the boundary anchoring enhances from panels (a) to (d). The polarity vector structure evolves from one that resembles the structure obtained using the Neumann BC to one that resembles the structure obtained using the Dirichlet BC, in which defects emerge.

Out-of-plane dynamics If we impose an in-plane Dirichlet boundary condition and begin with an initial condition with a nonzero p_3 component, for tumbling liquid crystals, then there could initially be defects near the boundaries, but later the director rotates out of plane to avoid formation of defects in the flow via a sequence of kayaking motions at different locations across the shear cell. Eventually, the solution will converge to a spatially inhomogeneous out-of-plane steady state. Figure 7 depicts the solution in space and time, as well as at a few selected spatial locations, as functions of time, respectively.

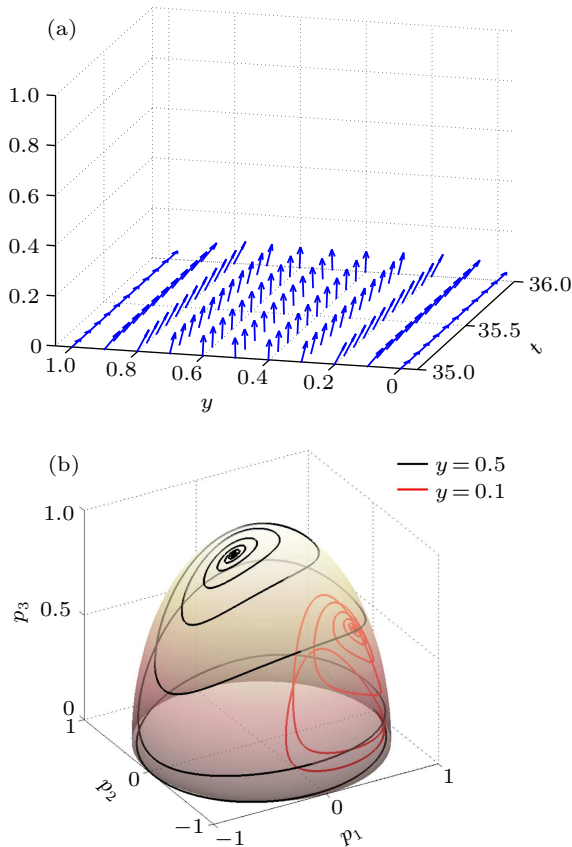


Fig. 7. Out-of-plane solutions for a tumbling ALC. Here, $v = 0.5$, Dirichlet BC. (a) The polarity vector in 3D as p_3 is perturbed away from zero. (b) Orbits of polarity vectors at $y = 0.1, 0.5$, respectively, traced from the beginning. Steady states in 3D are obtained.

When the Dirichlet boundary condition or soft anchoring boundary condition with small λ_b is used, the solution tends to tilt out of plane initially and it then undergoes kayaking motion in time for a while. Eventually, it may settle down to an out-of-plane steady state solution aligned to an out-of-plane direction. The reason for the solution to go out-of-plane is due to the fact that the material tries to avoid a defect where energy tends to be large. When the Dirichlet boundary condition or soft anchoring boundary condition with small λ_b is imposed at the boundary, the interior tumbling motion is in conflict with the aligned boundary condition, which can lead to defects if confined in the (x, y) space.

When the boundary condition is the Neumann BC or the soft anchoring boundary condition with large λ_b . The planar solutions are shown to be stable to small perturbations to p_3 . That the tumbling solution stays in-plane subject to small perturbations is a reflection of the fact that there is no defect in the unperturbed tumbling solution, so that the solution does not need to go out-of-plane to avoid paying an energy penalty. The addition of the distortional elasticity and the weak anchoring BC fails to select one or two time-periodic solutions among the infinitely many time-period kayaking solutions and the logrolling steady state, which sets this model prediction in this case, apart from that of the Ericksen–Leslie theory.

Figure 8 shows the evolution of the free energy density with the Dirichlet boundary condition. By comparing the free energy of the system in 2D and in 3D, we indeed notice that the free energy is smaller in the 3D solution when defects are absent. The time average of total energy $F_T(t)$ is defined as $F_T(t) = \frac{1}{t} \int_0^t F(s) ds$, where $F(t) = \int f(\mathbf{p}, \nabla \mathbf{p}) d\mathbf{x}$ is the total free energy at time t , $f(\mathbf{p}, \nabla \mathbf{p})$ is the free energy density at position \mathbf{x} and at time t .

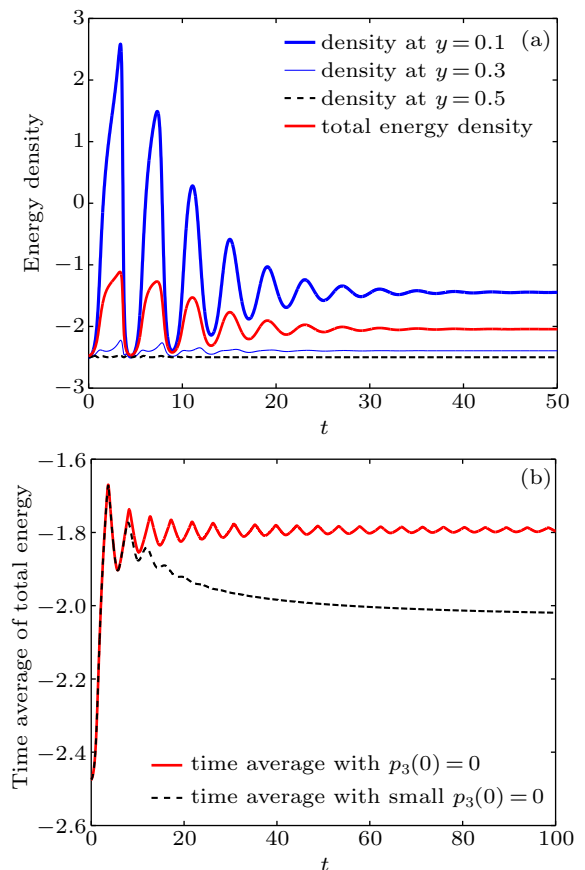


Fig. 8. Energy evolution in time with the Dirichlet BC. By going out-of-plane, the system attains a lower energy level by avoiding defects. (a) Free energy density with a small perturbation to p_3 in 3D and (b) Time average of the total free energy for the two cases.

In summary, the defect-free 1D spatial–temporal structure of the active liquid crystal system in steady shear subject

to the Dirichlet boundary condition is stable with respect to perturbations in p_3 ; the one that contains spatial-temporal defects is unstable subject to perturbations in p_3 . The unstable planar solution eventually attains the minimal energy, steady state by going to 3D to avoid defects. This scenario applies to the case of strong anchoring and soft anchoring with a small λ_b . When the boundary conditions are the Neumann boundary condition or the soft anchoring condition with a large λ_b , structures in the bulk dominate. In the latter case, solutions depend strongly on the initial conditions so that the limiting regime admits infinitely many long-time solutions, which is an artifact of the limiting regime. We next study the response dynamics in the nonlinear Poiseuille flow, where the velocity field is given by $\mathbf{v} = (Pe y(1-y), 0, 0)$ and Pe is a constant related to the pressure gradient.

4.2.1. Poiseuille flow

In a Poiseuille flow field, $\partial v_1 / \partial y = Pe(1-2y)$ attains zero at $y = 0.5$ and is nonzero elsewhere. Therefore, the local shear rate is zero at $y = 0.5$ and nonlinear at either side of $y = 0.5$. In planar solutions we can observe defects in the middle of the region in the tumbling case ($|v| < 1$) with respect to both the Dirichlet and Neumann boundary conditions. For the Dirichlet boundary condition, an additional pair of defects near the boundaries are also present periodically (see Fig. 9). For the flow aligning case ($|v| > 1$), there are no defects with respect to the two types of boundary conditions, as expected.

These planar solutions of defects with the Dirichlet BC

are all unstable with respect to perturbations in p_3 , which is analogous to the situation in shear flows. The stable 3D spatial-temporal structures corresponding to the planar solutions with defects are spatially inhomogeneous, out-of-plane steady states. Figure 10(d) depicts a transient solution in its final stage approaching an out-of-plane steady state.

For nonplanar solutions with the Neumann BC in the tumbling case ($|v| < 1$), the final state is a steady logrolling state $\mathbf{p} = (0, 0, \pm 1)$ depending on the initial condition shown in Fig. 10(b). Therefore, the nonlinear flow field selects two logrolling states among the infinitely many existing kayaking orbits in the limiting case. In the flow-aligning case ($|v| > 1$), the final state is in-plane flow-aligning, as shown in Fig. 9(c), with $p_3 = 0$. There is no sustaining time periodic kayaking solution for Poiseuille flow with both BCs.

As described above for the case under shear, there are transient defects forming in time briefly, but while \mathbf{p} points out of (x, y) -plane, the defects will disappear and the free energy becomes smaller than when defects are present in plane. The free energy is larger in the region near the boundary than that in the other region due to the Dirichlet BC. The transient defects in the centerline is a distinctive feature that differentiates this problem from the shear flow problem, where the free energy is the largest in the centerline. The Poiseuille flow field is in general a stronger flow than the shear flow due to its nonlinearity. The results presented above show that it can in fact select a pair of final steady states for tumbling ALCs, even for weak anchoring conditions.

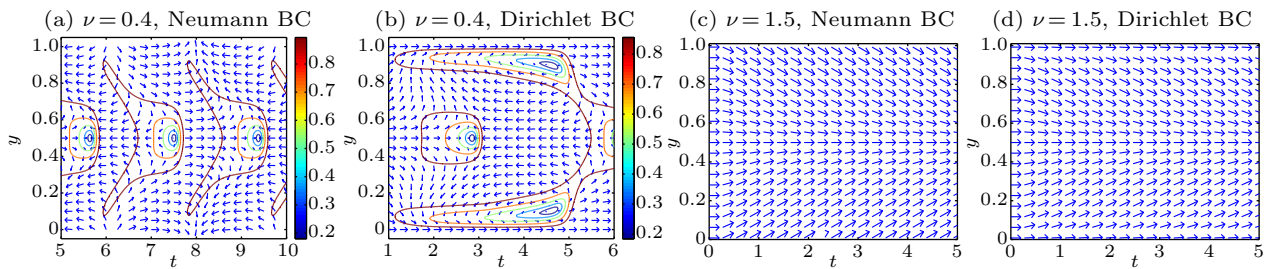


Fig. 9. Planar polarity vector structures with the two types of BCs and tumbling and flow-aligning ALCs at $Pe = 8$. (a) The polarity vector structure of tumbling ALCs with the Neumann BC. (b) The polarity vector structure of flow-aligning ALCs with the Dirichlet BC. (c) The structure of flow-aligning ALCs with the Neumann BC. (d) The structure of flow-aligning ALCs with the Dirichlet BC. Defects emerge in tumbling ALCs for all anchoring conditions in Poiseuille flows.

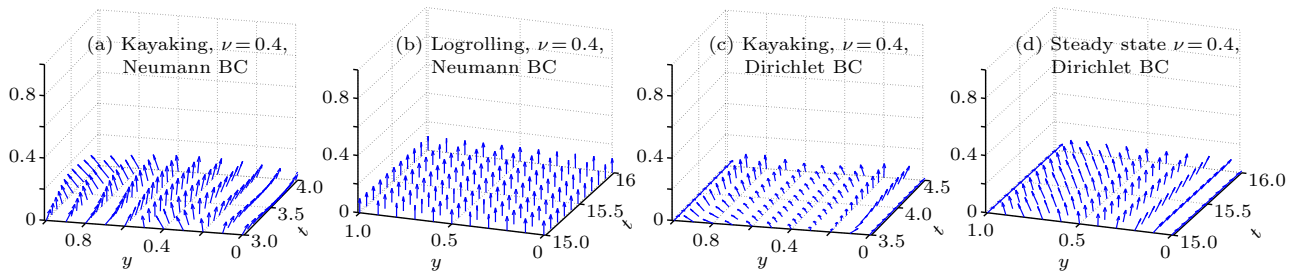


Fig. 10. Transient kayaking as well as final steady state structures for tumbling ALCs with respect to both the Neumann and Dirichlet BC, respectively. (a) Transient structure for $3 \leq t \leq 4$. (b) Steady state structure. (c) Transient structure for $3.5 \leq t \leq 4.5$. (d) Steady state structure. The 3D steady state structures are defect-free.

5. 1D inhomogeneous structures in ALC systems

Finally, we study spatial and temporal structures that vary in $y \in [0, 1]$ while homogeneous in (x, z) plane in the full model. From the incompressibility condition and the no-slip boundary condition on v_2 , we deduce $v_2 = 0$. Then, pressure Π is determined by the equation for v_2

$$\Pi = 2\beta \frac{\partial p_2}{\partial y} + \zeta p_2^2 - v p_2 h_2 - \int_0^y \frac{\partial \mathbf{p}}{\partial y} \cdot \mathbf{h} dy + \Pi_0, \quad (47)$$

where Π_0 is a constant pressure. The 1D equations for the other two velocity components and the components of the polarity vector are given by

$$\begin{aligned} \frac{\partial v_1}{\partial t} &= \eta \frac{\partial^2 v_1}{\partial y^2} + \beta \frac{\partial^2 p_1}{\partial y^2} + \zeta \frac{\partial(p_1 p_2)}{\partial y} \\ &\quad - v \frac{\partial}{\partial y} ((h_1 - h_2 \|\mathbf{p}\|^2) p_1 p_2) - \frac{(v-1)K_1}{2} \frac{\partial}{\partial y} \left(p_1 \frac{\partial^2 p_2}{\partial y^2} \right) \\ &\quad - \frac{(v+1)K_3}{2} \frac{\partial}{\partial y} \left(p_2 \frac{\partial^2 p_1}{\partial y^2} \right), \\ \frac{\partial v_3}{\partial t} &= \eta \frac{\partial^2 v_3}{\partial y^2} + \beta \frac{\partial^2 p_3}{\partial y^2} + \zeta \frac{\partial(p_3 p_2)}{\partial y} \\ &\quad - v \frac{\partial}{\partial y} ((h_1 - h_2 \|\mathbf{p}\|^2) p_3 p_2) - \frac{(v-1)K_1}{2} \frac{\partial}{\partial y} \left(p_3 \frac{\partial^2 p_2}{\partial y^2} \right) \\ &\quad - \frac{(v+1)K_3}{2} \frac{\partial}{\partial y} \left(p_2 \frac{\partial^2 p_3}{\partial y^2} \right), \\ \frac{\partial p_1}{\partial t} &= \frac{1}{\gamma} \left(K_3 \frac{\partial^2 p_1}{\partial y^2} + (h_1 - h_2 \|\mathbf{p}\|^2) p_1 \right) - \omega p_2 \frac{\partial p_1}{\partial y} \\ &\quad + \frac{v+1}{2} \frac{\partial v_1}{\partial y} p_2, \\ \frac{\partial p_2}{\partial t} &= \frac{1}{\gamma} \left(K_1 \frac{\partial^2 p_2}{\partial y^2} + (h_1 - h_2 \|\mathbf{p}\|^2) p_2 \right) - \omega p_2 \frac{\partial p_2}{\partial y} \\ &\quad + \frac{v-1}{2} \left(\frac{\partial v_1}{\partial y} p_1 + \frac{\partial v_3}{\partial y} p_3 \right), \\ \frac{\partial p_3}{\partial t} &= \frac{1}{\gamma} \left(K_3 \frac{\partial^2 p_3}{\partial y^2} + (h_1 - h_2 \|\mathbf{p}\|^2) p_3 \right) - \omega p_2 \frac{\partial p_3}{\partial y} \\ &\quad + \frac{v+1}{2} \frac{\partial v_3}{\partial y} p_2. \end{aligned} \quad (48)$$

We consider only two types of boundary conditions for \mathbf{p} , the Dirichlet BC (DBC) ($\mathbf{p}|_{y=0,1} = \mathbf{p}_0$) and the Neumann BC (NBC) ($\partial \mathbf{p} / \partial y = \mathbf{0}$) together with the no-slip BC for \mathbf{v} ($\mathbf{v}|_{y=0,1} = \mathbf{0}$).

Before we proceed to solve the initial boundary value problems, we identify the solution symmetries inherent in the governing system of equations in the following, which enables us to reduce our investigations to a smaller model parameter space.

1) $(p_1, p_2, p_3, v_1, v_3) \leftrightarrow (p_1, p_2, -p_3, v_1, -v_3)$, that is, if p_1, p_2, p_3, v_1, v_3 satisfy the equation, then so do $p_1, p_2, -p_3, v_1, -v_3$. This states a reflective symmetry in both the polarity vector and the flow field with respect to the (x, y) plane for all model parameters. Although, this symmetry may be limited

by the Dirichlet boundary condition on p_3 and v_3 .

2) $(p_1, p_2, p_3, v_1, v_3) \leftrightarrow (-p_1, p_2, p_3, -v_1, v_3)$. This is an analogous reflective symmetry for both the polarity vector and the flow field about the (y, z) plane for all model parameters. This symmetry is limited by the Dirichlet boundary condition on p_1 and v_1 . For a nonzero plane shear in v_1 , it is broken for sure. For channel flows, the symmetry is respected by the Neumann BC on \mathbf{p} .

3) $(p_1, p_2, p_3, v_1, v_3) \leftrightarrow (p_3, p_2, p_1, v_3, v_1)$. This is a third reflective symmetry for both the polarity vector and the flow field about a plane dividing the first quadrant in (x, z) plane for all model parameters. The Dirichlet boundary conditions can forbid the symmetry.

4) $(p_1, p_2, p_3, v_1, v_3, -\beta, -\omega) \leftrightarrow (p_1, -p_2, p_3, -v_1, -v_3, \beta, \omega)$. This shows that changing the sign of β and ω simultaneously can inflict a reflection of the polarity vector about the (x, z) plane and a completely reversed velocity field. This symmetry is broken in nonzero boundary conditions in v_1 ; for example, in the plane shear flow. However, this symmetry is respected for channel flows with a Neumann BC for \mathbf{p} .

5) $(p_1, p_2, p_3, v_1, v_3, -\beta, -\omega) \leftrightarrow (p_1, -p_2, -p_3, -v_1, v_3, \beta, \omega)$. This indicates that the sign change in β and ω simultaneously can inflict a reflection of \mathbf{p} about the x axis and reflection of velocity about the (y, z) plane. This symmetry is broken in nonzero boundary conditions in v_1 and some Dirichlet BCs for \mathbf{p} .

6) $(p_1, p_2, p_3, v_1, v_3, -\beta, -\omega) \leftrightarrow (-p_1, -p_2, p_3, v_1, -v_3, \beta, \omega)$. This indicates that the sign change in β and ω simultaneously can inflict a reflection of \mathbf{p} about the z axis and reflection of velocity about the (x, y) plane. This symmetry survives in the simple shear flow with the Neumann BC for \mathbf{p} , but is broken when the BC for \mathbf{p} is Dirichlet.

7) $(p_1(y, t), p_2(y, t), p_3(y, t), v_1(y, t), v_3(y, t), -\beta, -\omega) \leftrightarrow (p_1(1-y, t), p_2(1-y, t), p_3(1-y, t), -v_1(1-y, t), -v_3(1-y, t), \beta, \omega)$. This shows a symmetry about the flow centerline for the polarity vector and antisymmetry for the velocity field while the sign of β and ω are changed simultaneously. Although, the existence of the solution symmetry is limited by the boundary conditions on \mathbf{p} and \mathbf{v} .

8) $(p_1, p_2, 0, v_1, 0, -\zeta, -v) \leftrightarrow (p_2, p_1, 0, -v_1, 0, \zeta, v)$ at $\beta = 0$. When the active viscous stress is absent, there is a symmetry between a discotic puller and a rod pusher ALC system, in which the corresponding velocities are opposite. An analogous symmetry exists between a discotic pusher and a rod puller ALC pair.

9) In the limit of $\beta = \omega = 0$, where the system describes an apolar ALC, a reflective symmetry between \mathbf{p} and $-\mathbf{p}$ exists.

We note that these solution symmetries are given independent of the imposed boundary conditions. When boundary conditions are imposed in both \mathbf{p} and \mathbf{v} , some of these symmetries may be forbidden.

For the ALC system, we are interested in the emergence of spontaneous flows and their time evolution. The existence of spontaneous flows in active liquid crystals was first identified by Voituriez *et al.* for inertialess models without active stress (i.e., $\beta = 0$).^[32] They predicted that there is a spontaneous flow transition from a homogeneously polarized immobile state to a perturbed flowing state, in a one-dimensional geometry. The critical value of the activity ζ_c for the transition is determined analytically by linearizing the equations of motion around a specific initial state.^[32] In Ref. [46], Edwards *et al.* gave a complete characterization of the phase space for both contractile and extensile particles moving in a narrow channel as a function of the parameter pair (ζ, ν) and the initial orientation. In that paper, they assumed $\|\mathbf{p}\| = 1, \lambda = \beta = \omega = 0$, and for each initial orientation, identified six different parametric regions in (ζ, ν) -space for six different types of flow and orientational structures.

In this section, we study how spontaneous flows evolve nonlinearly after its onset, in the presence of the active viscous stress, and how external shear impact on the spatial-temporal structure originated from the spontaneous flow in 1D space.

5.1. Planar structures formed by spontaneous flows

5.1.1. Planar structures without the active viscous stress and the self-propelled velocity

The onset of spontaneous flows is predicted by a linear instability analysis of the constant equilibrium state. In this subsection, we would like to examine the time evolution of the spontaneous flows by solving the nonlinear governing system of equations with appropriate boundary conditions numerically in space and time. We focus on a 2D confined orientation of \mathbf{p} with the Dirichlet BC for both \mathbf{p} and \mathbf{v} , firstly, where we explore the spatial-temporal structure formation using two special initial states for \mathbf{p} specifically

$$\begin{aligned} \text{(i)} \quad & \mathbf{p}(y, t=0) = (1, \delta \sin(k\pi y), 0), \\ \text{(ii)} \quad & \mathbf{p}(y, t=0) = (\delta \sin(k\pi y), 1, 0), \end{aligned} \quad (49)$$

where k is an integer representing the wave number and $\delta = 10^{-2}$ is used throughout the paper, measuring the amplitude of the perturbation. An analysis on an inertialess limit of the model suggests that the spontaneous flow emerges if $\zeta(\nu - 1) < \zeta_c^1(\nu - 1) < 0$ for initial state (i), and if $\zeta(\nu + 1) < \zeta_c^2(\nu + 1) < 0$ for initial state (ii), with two different critical values ζ_c^1 and ζ_c^2 at a given molecular shape determined by

ν . When the above parametric condition is met, the small initial disturbance can generate a spontaneous flow, which eventually evolves into a steady state structure in both \mathbf{p} and \mathbf{v} . Let us take look at the structures at $\beta = \omega = 0$ firstly. Figure 11 depicts a set of steady, spatial structures formed by the polarity vector, as well as the flow after a long time due to a spontaneous flow, where Dirichlet BCs consistent with the two initial states are enforced on \mathbf{p} , respectively, and the no-slip boundary condition is enforced on \mathbf{v} at the boundaries. Figures 11(a) and 11(b) show the steady structure of the polarization field \mathbf{p} using the first initial state with $k = 1$ and $k = 2$, respectively, where figures 11(e) and 11(f) are the accompanying velocity profiles of v_1 . In the two simulations, ALCs are consisted of rodlike puller molecules $\zeta > 0$. In Fig. 11(a), the flow moves to the polarity vector direction in the lower half of the channel while against it in the upper half, creating a nonlinear shear flow field in a large part of the channel in the middle. In Fig. 11(b), the flow moves completely against the polarity vector direction with a minimum at the location where the polarity vector is perfectly aligned to the wall. Because of the mismatched motion between the mean fluid flow and the individual active molecules, a force balance is attained to allow the existence of the flow and orientational structures in steady states. In steady states, we simplify the governing equation for velocity component v_1 as follows:

$$\begin{aligned} 0 = & \eta \frac{\partial^2 v_1}{\partial y^2} + \beta \frac{\partial^2 p_1}{\partial y^2} + \zeta \frac{\partial(p_1 p_2)}{\partial y} \\ & + \gamma \left[\frac{(\nu - 1)^2}{4} p_1^2 + \frac{(\nu + 1)^2}{4} p_2^2 \right] \frac{\partial v_1}{\partial y}. \end{aligned} \quad (50)$$

This equation relates the local maximum or minimum of the velocity component v_1 to the rotational direction of the polarity vector. At an extremum, the equation reduces to

$$\frac{d^2 v_1}{dy^2} = -\frac{\zeta}{\eta} \frac{d(p_1 p_2)}{dy}. \quad (51)$$

In all our simulations, we observe only two types of polarity vector orientation that yield local extrema in v_1 . One is horizontal and the other vertical relative to the boundary. We parametrize $p_1 = r \cos \theta$, $p_2 = r \sin \theta$ with $\theta = 0, \pi/2$ corresponding to the horizontal and vertical polarity vector orientations, respectively. We assume r does not change much during the rotation. Then,

$$\frac{d(p_1 p_2)}{dy} \approx r^2 \cos(2\theta) \frac{d\theta}{dy}.$$

If $d\theta/dy > 0$ (\mathbf{p} rotates counterclockwise), then v_1 is at a local maximum at $(\zeta > 0, \theta = 0)$ or $(\zeta < 0, \theta = \pi/2)$ and local minimum at $(\zeta < 0, \theta = 0)$ or $(\zeta > 0, \theta = \pi/2)$. On the other hand, if $d\theta/dy < 0$ (\mathbf{p} rotates clockwise), then v_1 is at a local minimum at $(\zeta > 0, \theta = 0)$ or $(\zeta < 0, \theta = \pi/2)$ and local

maximum at $(\zeta < 0, \theta = 0)$ or $(\zeta > 0, \theta = \pi/2)$. This simple diagnostic measure will be used to assist us to interpret the relationship between the polarity vector and the coupled velocity field in the rest of the paper.

In Fig. 11(a), near the bottom of the channel, the polarity vector transitions from parallel to a tilted orientation relative to the wall via a counterclockwise rotation. This leads to a local maximum in the velocity component v_1 at about $y = 0.1$, creating a flow field that resembles a spurt phenomenon in polymeric liquid. Near the top of the channel, the polarity vector transitions back to the parallel position via a clockwise rotation. This leads to a local minimum in the velocity component

v_1 at $y = 0.9$, resembling a reversed spurt flow. In Fig. 11(b), the spurt flow phenomenon is only observed in the middle of the channel through a local minimum in v_1 at $y = 0.5$, which flows opposite to the direction of the polarity vectors.

Figures 11(c) and 11(d), as well as figures 11(g) and 11(h), depict the polarity vector as well as the accompanying velocity component v_1 for the second initial state at $k = 1$ and $k = 2$, respectively. Here, ALCs consist of discotic pusher molecules. The patterns of mean fluid flows in the discotic The ALCs are completely opposite to those in the rodlike ALCs, consistent with symmetry #8 identified above.

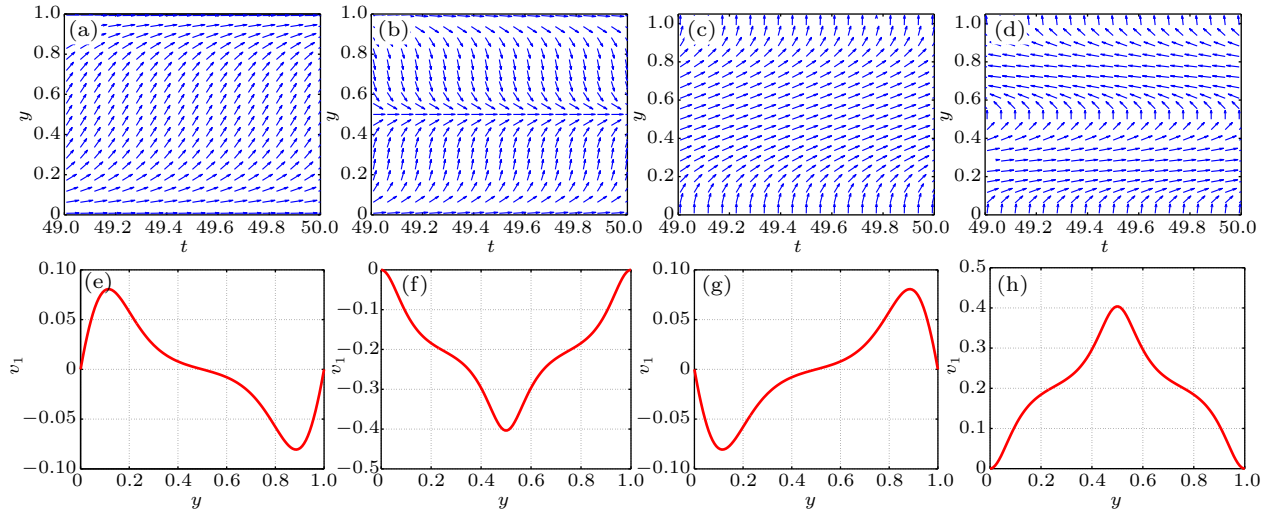


Fig. 11. Steady states of spontaneous flows for tumbling ALCs, where Dirichlet BCs are used on \mathbf{p}, \mathbf{v} for the two initial states, respectively. The parameters are $K_1 = K_3 = 0.01, h_1 = h_2 = 10, \gamma = 1, \omega = 0, \lambda = 0, \eta = 1, \beta = 0$. The steady states correlate with the initial orientational structures. The velocity is the largest at the well-aligned area for the rod ((e) and (f)) and the discotic ((g) and (h)) ALC. Panels (c), (d), (g), and (h) can be obtained from panels (a), (b), (e), and (f) via symmetry #8 mentioned in the text. The initial states and other parameters are: (a) initial state (i), $\zeta = 4, v = 0.5, k = 1$, (b) initial state (i), $\zeta = 4, v = 0.5, k = 2$, (c) initial state (ii), $\zeta = -4, v = -0.5, k = 1$, (d) initial state (ii), $\zeta = -4, v = -0.5, k = 2$, (e) initial state (i), $\zeta = 4, v = 0.5, k = 1, T = 50$, (f) initial state (i), $\zeta = 4, v = 0.5, k = 2, T = 50$, (g) initial state (ii), $\zeta = -4, v = -0.5, k = 1, T = 50$, (h) initial state (ii), $\zeta = -4, v = -0.5, k = 2, T = 50$.

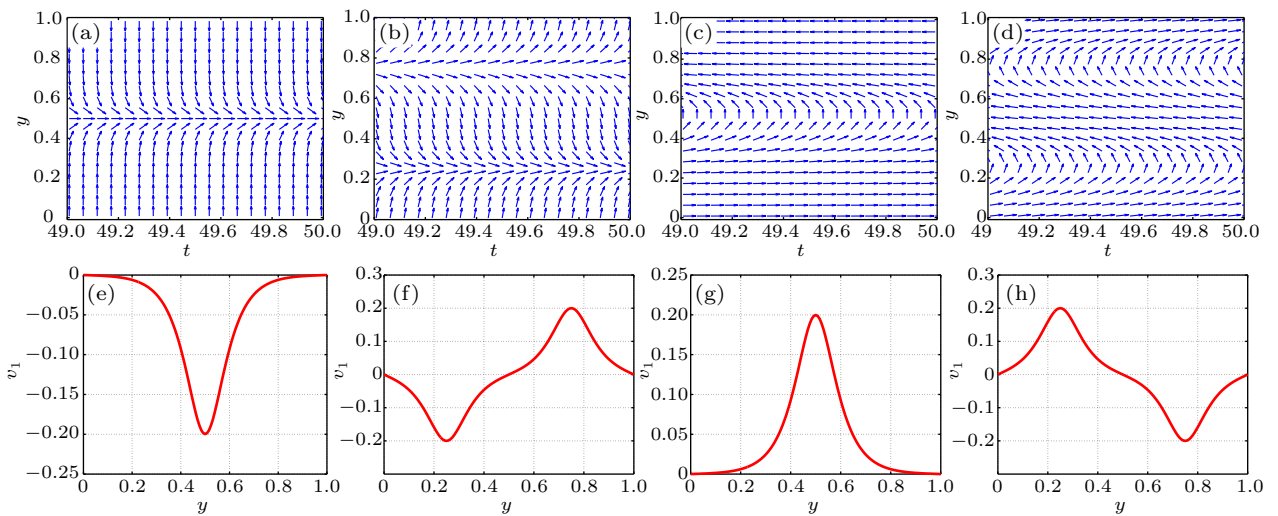


Fig. 12. Steady states of spontaneous flows for tumbling ALCs, where the Neumann BC is used on \mathbf{p} and the non-slip BC on \mathbf{v} for the two initial states, respectively. The parameter values are $K_1 = K_3 = 0.01, h_1 = h_2 = 10, \gamma = 1, \omega = 0, \lambda = 0, \eta = 1, \beta = 0$. The final steady states correlate with the initial orientational structures. The magnitude of the velocity is the largest at the well-aligned area for the rod ((e) and (f)) and the discotic ((g) and (h)) ALC, consistent with the intuition. We note that the Neumann BC seems to prefer the boundary orientation in steady state perpendicular to the orientation of the polarity vector in the initial state. The initial states and other parameters are: (a) initial state (iii), $\zeta = 4, v = 0.5, k = 1$, (b) initial state (iii), $\zeta = 4, v = 0.5, k = 2$, (c) initial state (iv), $\zeta = -4, v = -0.5, k = 1$, (d) initial state (iv), $\zeta = -4, v = -0.5, k = 2$, (e) initial state (iii), $\zeta = 4, v = 0.5, k = 1, T = 50$, (f) initial state (iii), $\zeta = 4, v = 0.5, k = 2, T = 50$, (g) initial state (iv), $\zeta = -4, v = -0.5, k = 1, T = 50$, (h) initial state (iv), $\zeta = -4, v = -0.5, k = 2, T = 50$.

If we use the Neumann BC for \mathbf{p} at the boundaries ($\partial \mathbf{p} / \partial y|_{y=0,1} = 0$), then we compute the solutions using two special initial states: (iii) $\mathbf{p}(y, t = 0) = (1, \delta \cos(k\pi y), 0)$ and (iv) $\mathbf{p}(y, t = 0) = (\delta \cos(k\pi y), 1, 0)$, where k is an integer representing the wave number. For the Neumann BC on \mathbf{p} , many symmetries identified apply; the criterion for the formation of spontaneous flow is also given by $\zeta(v - 1) < \zeta_c^1(v - 1) < 0$ for initial state (iii), or by $\zeta(v + 1) < \zeta_c^2(v + 1) < 0$ for initial state (iv), with two different critical values $\zeta_c^{1,2}$, respectively. The orientational structures and the flow structures are different from those obtained from the simulations with the corresponding Dirichlet BC though (see Fig. 12). From a linear stability analysis we have learned that the unstable component of the polarity vector in the model with this boundary condition is p_2 . Although the initial orientation of \mathbf{p} is parallel to the wall with the initial state (iii), the p_2 component evolves to an orientation perpendicular to the boundary in the steady state, which is shown in Figs. 12(a) and 12(b). Likewise, in the initial state (iv), the unstable component of \mathbf{p} is p_1 , so that it evolves to a steady state parallel to the wall. For pullers shown in Figs. 12(e) and 12(f), a negative velocity local minimum correlates with a converging rodlike molecular orientation with respect to the x direction (clockwise rotation); whereas a positive local maximum velocity component correlates with a diverging rodlike molecular orientation rel-

ative to the x axis (counterclockwise rotation). For discotic pushers, a positive velocity maximum correlates with a 180°-counterclockwise rotated bending structure while a negative velocity minimum correlates with a 180°-clockwise rotated bending structure in the channel, as shown in Figs. 12(g) and 12(h). The local maximum or minimum velocity component v_1 represents a spurt flow (relative to the mean flow) in the channel, which correlates with the localized, enhanced polarity orientation.

When the Neumann BC is used, there could exist more bending structures of a 180° rotation in the polarity vector determined by the wave integer in the initial state at any given, large, activity parameter $|\zeta|$.^[56] Figures 13(a)–13(d) depict a simulation with a large $|\zeta|$ that can accommodate more such bending structures. Essentially, the initially given wave integer determines the final bending structures in the steady states in long-time simulations. However, this scenario seems not to be upheld in the solution with the Dirichlet BC.

For the system with the Dirichlet BC and initial states: $\mathbf{p} = (1, \delta \sin(4\pi y), 0)$ and $\mathbf{p} = (\delta \sin(4\pi y), 1, 0)$, we solve the equations for the long-time behavior of the solutions generated by spontaneous flows and contrast the simulations with and without the inertia effect $\partial \mathbf{v} / \partial t$. We observe that, when we ignore the inertia term and $|\zeta|$ is sufficiently large, the number

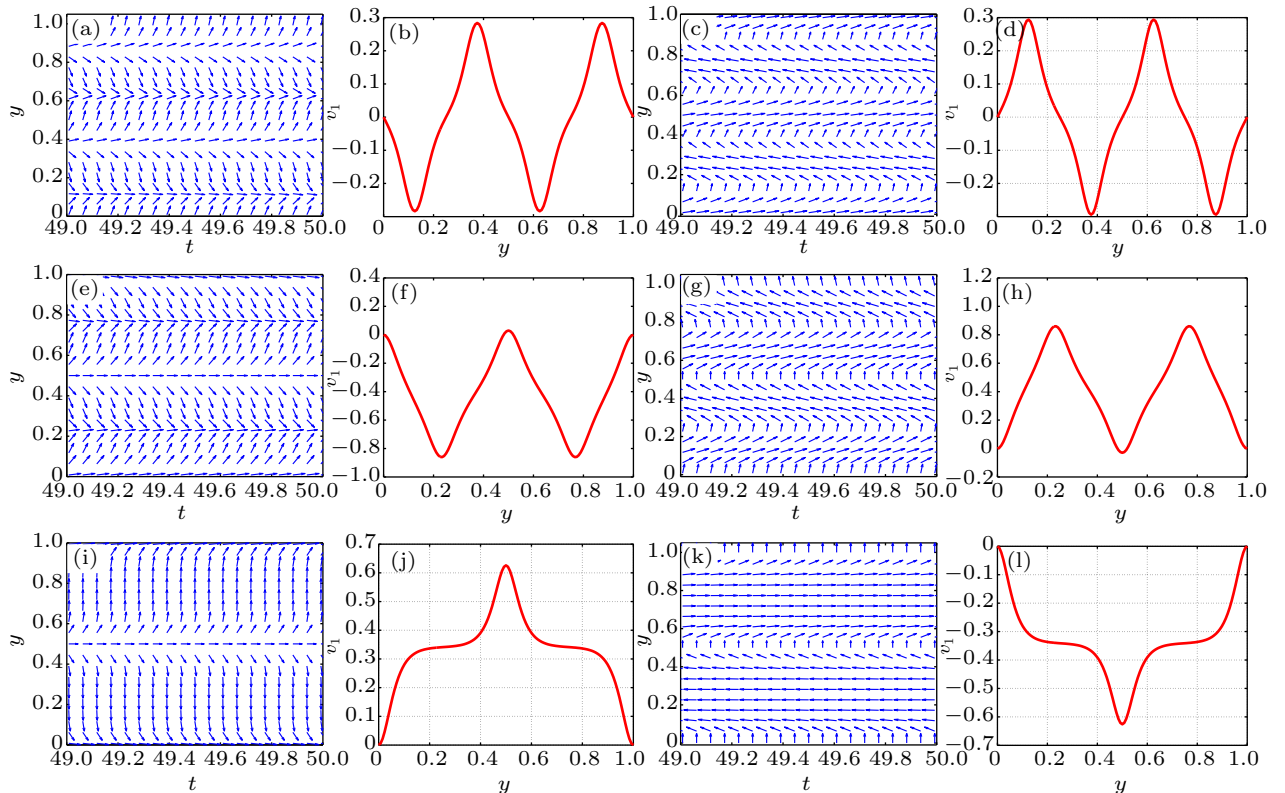


Fig. 13. Steady states of spontaneous flows for tumbling ALCs for the two initial states, respectively. The parameter values are $K_1 = K_3 = 0.01, h_1 = h_2 = 10, \gamma = 1, \omega = 0, \lambda = 0, \eta = 1, \beta = 0$. (a)–(d) The Neumann BC is used on \mathbf{p} . (e)–(h) The Dirichlet BC is used on \mathbf{p} in the inertialess limit. (i)–(l) The Dirichlet BC is used on \mathbf{p} . Inertia seems to have the “wave-limiting” ability to favor bending structures of long-wave features in the steady state. The initial states and other parameters are: (a) initial state (iii), $\zeta = 10, v = 0.5, k = 4$, (b) initial state (iii), $\zeta = 10, v = 0.5, k = 4, T = 50$, (c) initial state (iv), $\zeta = -10, v = -0.5, k = 4$, (d) initial state (iv), $\zeta = -10, v = -0.5, k = 4, T = 50$, (e) initial state (i), $\zeta = 10, v = -0.5, k = 4$, (f) initial state (i), $\zeta = 10, v = -0.5, k = 4, T = 50$, (g) initial state (ii), $\zeta = -10, v = 0.5, k = 4$, (h) initial state (ii), $\zeta = -10, v = 0.5, k = 4, T = 50$, (i) initial state (i), $\zeta = 10, v = -0.5, k = 4$, (j) initial state (i), $\zeta = 10, v = -0.5, k = 4, T = 50$, (k) initial state (ii), $\zeta = -10, v = 0.5, k = 4$, (l) initial state (ii), $\zeta = -10, v = 0.5, k = 4, T = 50$.

of bending structures in the steady state correlates with the initial profile, as shown in Figs. 13(e)–13(h). This is consistent with the linear stability analysis for an inertialess limit.^[56] But if we retain the inertia term $\partial \mathbf{v} / \partial t$ in our numerical simulations, the results are different (see Figs. 13(i)–13(l)). Figures 13(i)–13(l) show that simulations beginning with the initial state of four bending structures in the channel eventually evolves into a structure with only two bending structures in the end. In fact, the steady state results obtained are exactly the results obtained with the initial state at $k = 2$. Inertia seems to have the function to disrupt the complex flow and orientational patterns to promote the structures of low wave numbers. This phenomenon warrants a more detailed study in the future.

We next investigate how the active viscous stress $\beta(\nabla \mathbf{p} + \nabla \mathbf{p}^T)$ affects the flow and orientational structure without an external driven mechanism.

5.1.2. Effect of active viscous stress to spontaneous flow

In some previous studies,^[46–49] $\omega = \beta$ was assumed in analogous models for ALCs. However, we will not impose such a constraint in this study. Figure 14 depicts a set of simulations with the Dirichlet BC and the first initial state at $k = 2$. In these simulations, spontaneous flows evolve into steady states at $T = 50$. One observes that the magnitude of

the velocity increases as $|\beta|$ increases. $\beta < 0$ promotes rapid transitions in the polarity vector orientation near the boundaries to create a flow field that looks like a plug flow. The boundary layers in the velocity field at the boundaries narrow as $|\beta|$ increases. $\beta > 0$ promotes a rapid transition in the polarity vector orientation in the middle of the channel to create an internal layer in the fluid flow. The internal layer narrows as β increases, so that the fluid flow spurts in the middle of the channel. There are no defects in the flow field during the time evolution.

In simulations with the second initial state $\mathbf{p} = (\delta \sin(\pi y), 1, 0)$ and the Dirichlet BC, the active viscosity β destroys the structure symmetry that exists at $\beta = 0$ and with the first initial state, especially, in the velocity field. Figure 15 depicts the numerical results for $\beta = -0.3, -0.1$, respectively. Comparing the results with those in Fig. 11, the broken symmetry in the structure is apparent. For this initial states, we can obtain the results for $\beta = 0.1, 0.3$, respectively, by invoking symmetry #7 listed above. The polarity vector and velocity correlation in the simulations once again follow the trend identified previously, in which a local minimum in the velocity component v_1 corresponds to a rapid clockwise polarity vector rotation while a local maximum corresponds to a rapid counterclockwise rotation in the polarity vector field.

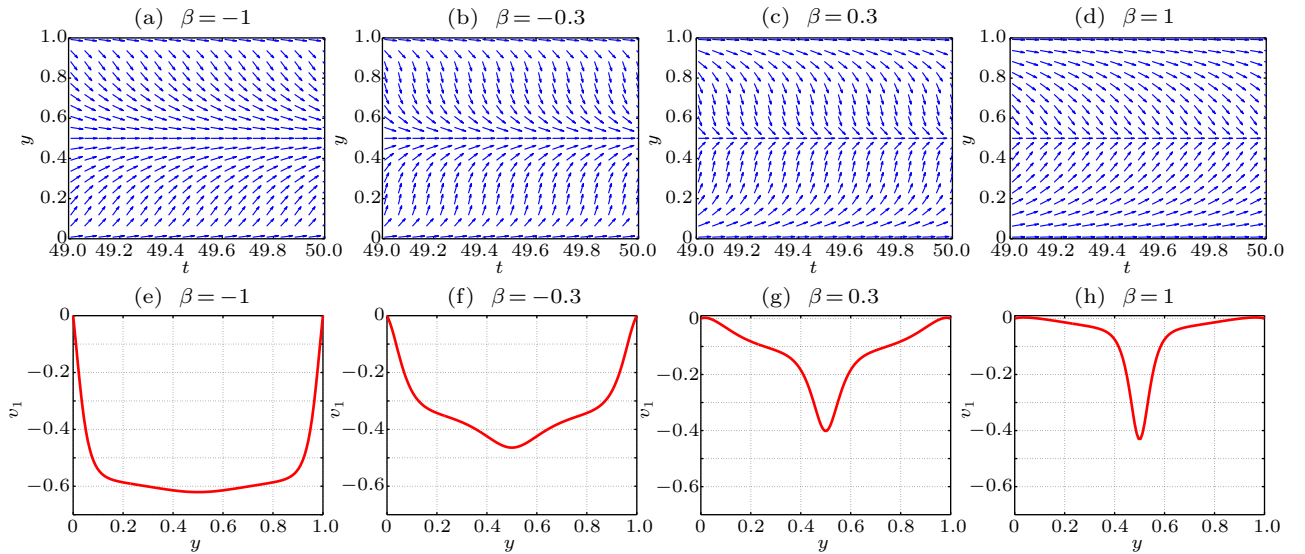


Fig. 14. Steady states at four selected values of active viscosity $\beta = -1, -0.3, 0.3, 0.1$ with the first initial state $\mathbf{p} = (1, \delta \sin(2\pi y), 0)$ and the Dirichlet BCs on \mathbf{p} and \mathbf{v} . The parameter values are $K_1 = K_3 = 0.01, h_1 = h_2 = 10, \gamma = 1, v = 0.5, \omega = 0, \zeta = 4$. The steady states are shown at time $T = 50$. A negative β makes the velocity field more homogeneous in the middle of the flow field, so that it looks like a plug flow at small β . A positive β retards the flow away from the centerline, so that a spurt phenomenon becomes more prominent at the centerline at a large β . Corresponding to the velocity field, we notice an enhanced orientational transition at the centerline of the polarity vector as β increases from negative to positive.

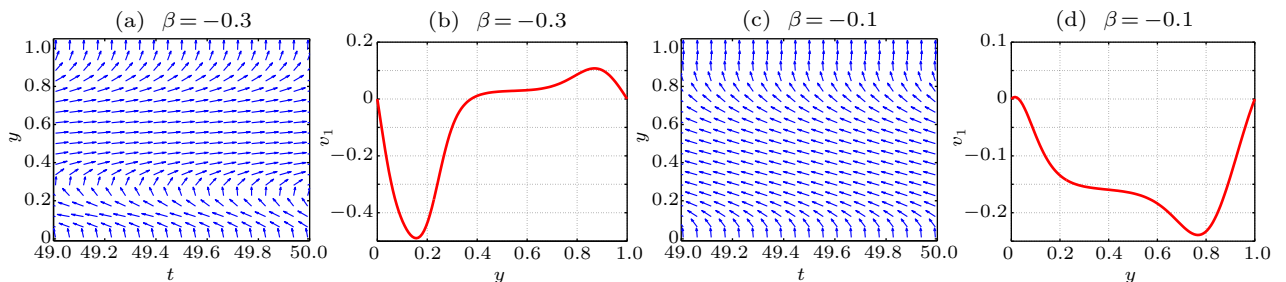


Fig. 15. Steady states at $\beta = -0.3, -0.1$ with the second initial state $\mathbf{p} = (0.01 \sin(\pi y), 1, 0)$ and Dirichlet BCs on \mathbf{p}, \mathbf{v} . The parameter values are $K_1 = K_3 = 0.01, h_1 = h_2 = 10, \gamma = 1, \omega = 0, v = -0.5, \zeta = -4$. Structural symmetry is broken in these solutions.

5.2. Interaction between shear and a spontaneous flow

In this subsection, we study how shear can impact on the spontaneous flow in its time evolution. Edwards *et al.*^[46] studied the polarity vector field coupled to a shear flow using the Neumann boundary condition for \mathbf{p} in the flow-tumbling regime ($|\nu| < 1$), where they noted that even a small amount of shear can cause the polarization field to rotate continuously so that there is no steady state; whereas, in the flow-aligning regime ($|\nu| > 1$) the steady state with spontaneous flow can survive in applied shear flows up to a certain shear rate.

Here, we consider the Dirichlet boundary condition for \mathbf{p} . We note that in the tumbling regime ($|\nu| < 1$) the steady state of a spontaneous flow can also survive in applied shear flows up to a certain shear speed, as in the flow-aligning regime ($|\nu| > 1$). Figure 16 depicts a simulation with the initial state $\mathbf{p}(y, t = 0) = (1, \delta \sin \pi y, 0)$, $\mathbf{v}(y, t = 0) = (Pe y, 0, 0)$. Figures 16(a)–16(c) and figures 16(e)–16(g) depict a series of steady states under three applied shear speeds that are all smaller than the critical shear speed Pe_c while figures 16(d) and 16(h) depict the unsteady state under shear with the given shear speed bigger than the critical shear speed Pe_c . When the shear speed Pe is small, the active stress dominates in the total stress, so that the solution evolves into a steady state in time, where, for instance, the velocity profile Fig. 16(e) has a local minimum and a local maximum located near the bottom and the top boundaries of the flow field, respectively, just as in the case without shear. When the shear speed exceeds the critical value Pe_c , shear dominates so that the tumbling behavior ensues in \mathbf{p} while the velocity profile Fig. 16(h) is nearly linear. In the steady state structure ($Pe < Pe_c$), the range of the rotational angle of \mathbf{p} field increases clockwise with the shear speed Pe . In unsteady states ($Pe > Pe_c$), \mathbf{p} field rotates continuously under shear and produces transient defects near the boundaries due to the Dirichlet boundary condition. In addition, shear can

break the orientational symmetry in the spontaneous flow with respect to the second initial states.

Next, we conduct numerical simulations to investigate the interplay between the active viscous stress and the shear flow. For initial state $\mathbf{p} = (1, 0, 0)$ with the Dirichlet BC, there exist critical values $\beta_c^n < 0$ and $\beta_c^p > 0$ such that if $\beta_c^n < \beta < \beta_c^p$, then \mathbf{p} is periodic with a spatial-temporal structure including transient defects. If $\beta > \beta_c^p$ or $\beta < \beta_c^n$, then \mathbf{p} eventually evolves into a steady state. Figure 17 depicts the numerical solutions with the prescribed initial state and at a few selected values of β . When the solution is in steady state, there exists a boundary layer of v_1 in $y \in (0, 0.1)$ for $\beta = 3$, where v_1 increases very quickly to near 4. The effective shear rate is generally small in $y > 0.1$ (see Fig. 17(d)). When we negate the sign of β , the boundary layer location is shifted to the opposite side of the flow region. In most parts of the region, flow velocity is small; it transitions to the prescribed boundary shear speed $Pe = 4$ in the boundary layer near $y = 1$. In general, the polarity vector structure flips when either the sign of β is changed or the orientation of the initial state is reversed (see Figs. 17(a)–17(c) and 17(e)–17(g)).

For initial conditions $\mathbf{p} = (0, \pm 1, 0)$, we obtain similar results. When $\beta_c^n < \beta < \beta_c^p$, there are spatial-temporal structures that may include time dependent defects. When $\beta > \beta_c^p$ or $\beta < \beta_c^n$, the solutions eventually approach steady states. At the steady state, the velocity v_1 has a boundary layer near $y = 1$ when $\beta = 4$ and initial state $\mathbf{p} = (0, 1, 0)$. If $\beta = -4$ and initial state $\mathbf{p} = (0, 1, 0)$, then the boundary layer of the velocity curve is near $y = 0$. Figure 18 depicts the spatial-temporal structure and the steady state at selected values of β , respectively. Changing the direction of the boundary condition on \mathbf{p} also alters the spatial-temporal structures and the location of the boundary layer.

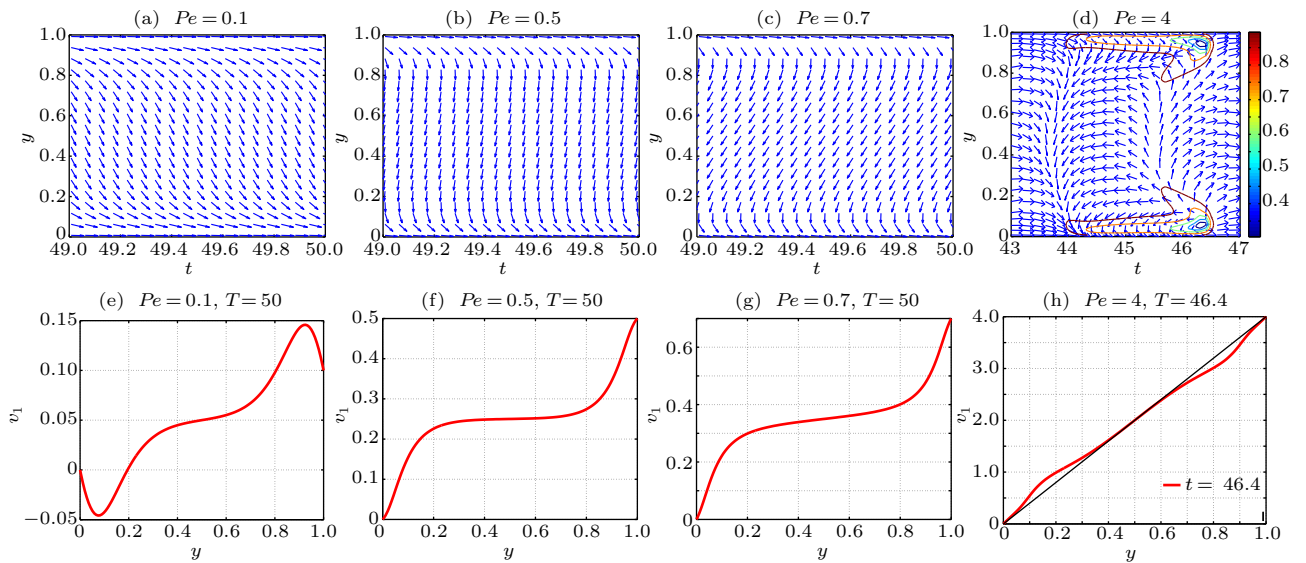


Fig. 16. Structures at four selected shear speeds $Pe = 0.1, 0.5, 0.7, 4$ with the first initial state $\mathbf{p} = (1, 0.01 \sin(\pi y))$ and Dirichlet BCs on \mathbf{p} and \mathbf{v} . The parameter values are $K_1 = K_3 = 0.01$, $h_1 = h_2 = 10$, $\gamma = 1$, $\nu = 0.5$, $\omega = 0$, $\lambda = 0$, $\eta = 1$, $\zeta = 4$, $\beta = 0$. The contour lines are based on $\|\mathbf{p}\|$. In panel (h), the velocity curve is at $T = 46.4$, when the defects emerge. (a)–(c) and (e)–(g) The active stress dominates so that a steady structure emerge in time. (d) and (h) The shear stress dominates so that a spatial-temporal structure emerges.

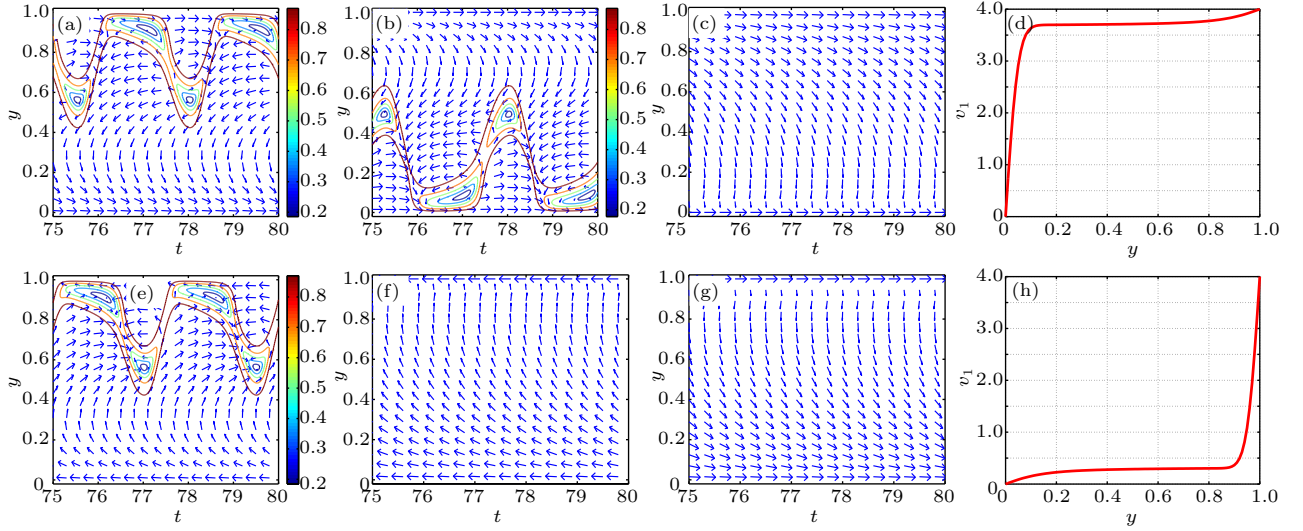


Fig. 17. Transient and steady structures of tumbling ALCs with the Dirichlet BC and the first initial state under shear. The parameter values are $Pe = 4$, $K_1 = K_3 = 0.04$, $h_1 = h_2 = 10$, $\gamma = 1$, $\omega = 0$, $\lambda = 0$, $\eta = 1$, $\nu = 0.5$, $\zeta = 1$. The contour lines are based on $\|\mathbf{p}\|$. Polarity structures are asymmetric with respect to y . Transient defect structures and the boundary layer can be located near the bottom of the flow field or on the top depending on the sign of β and the boundary anchoring condition. In steady states, the velocity field behaves like a plug flow with a boundary layer biased at one wall. Panels (a) and (e) and panels (f) and (g) pair according to symmetry #6, respectively. The parameters are: (a) $\mathbf{p}(y, 0) = (1, 0, 0)$, $\beta = -1$, (b) $\mathbf{p}(y, 0) = (1, 0, 0)$, $\beta = 1$, (c) $\mathbf{p}(y, 0) = (1, 0, 0)$, $\beta = 3$, (d) $\mathbf{p}(y, 0) = (1, 0, 0)$, $\beta = 3$, $T = 80$, (e) $\mathbf{p}(y, 0) = (-1, 0, 0)$, $\beta = 1$, (f) $\mathbf{p}(y, 0) = (-1, 0, 0)$, $\beta = 3$, (g) $\mathbf{p}(y, 0) = (1, 0, 0)$, $\beta = -3$, (h) $\mathbf{p}(y, 0) = (1, 0, 0)$, $\beta = -3$, $T = 80$.

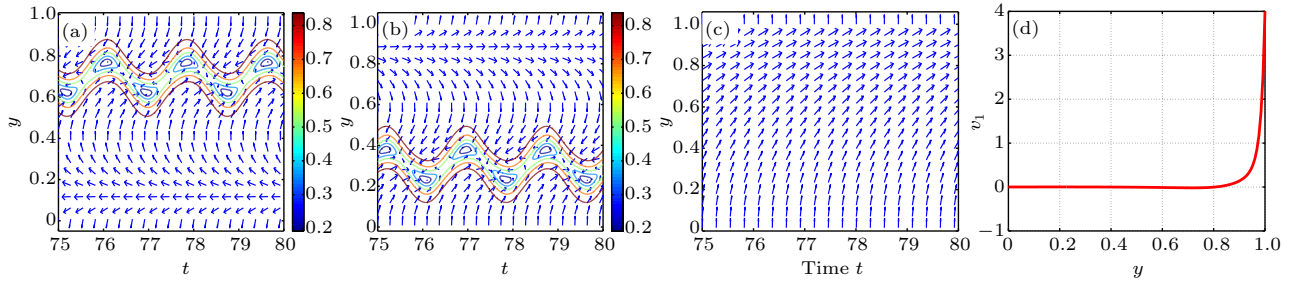


Fig. 18. Transient and steady structures of tumbling ALCs with the Dirichlet BC and the second initial state under shear. The parameter values are $Pe = 4$, $K_1 = K_3 = 0.04$, $h_1 = h_2 = 10$, $\gamma = 1$, $\omega = 0$, $\lambda = 0$, $\eta = 1$, $\nu = 0.5$, $\zeta = 1$. The contour lines are based on $\|\mathbf{p}\|$. The transient defect structures are pushed inward to the flow field because of the boundary condition, although still located at the bottom of the flow field or on the top depending on β and the BC. The boundary layer in the steady state is also near the wall at large β . Changing the direction of the boundary anchoring also flips the structure of the polarity vector upside down. The parameters are: (a) $\mathbf{p}(y, 0) = (0, -1, 0)$, $\beta = 1$, (b) $\mathbf{p}(y, 0) = (0, 1, 0)$, $\beta = 1$, (c) $\mathbf{p}(y, 0) = (0, 1, 0)$, $\beta = 4$, (d) $\mathbf{p}(y, 0) = (0, 1, 0)$, $\beta = 4$, $T = 80$.

5.3. Out-of-plane structures

We will next investigate the stability of the planar structures to perturbations in p_3 to explore which of the planar structures identified in previous sections can actually survive in 3D. We first consider the model prediction ignoring the active viscous stress and self-propelled velocity (i.e., $\omega = \beta = 0$.)

5.3.1. Spontaneous flow structures

Firstly, we consider the initial state $\mathbf{p} = (1, \delta p_2, \delta p_3)$ with the Dirichlet BC $\mathbf{p}|_{y=0,1} = (1, 0, 0)$ or the Neumann BC $\partial \mathbf{p} / \partial y|_{y=0,1} = (0, 0, 0)$. Our numerical computations show that for the two types of BCs, the system is stable in p_3 direction; that is, the spontaneous flow initiated near the 2D plane stays in $(p_1, p_2, 0)$ plane. This is consistent with the result of a linear stability analysis for an inertialess limit.^[56]

Secondly, for the initial state $\mathbf{p} = (\delta p_1, 1, \delta p_3)$ with the Dirichlet BC $\mathbf{p}|_{y=0,1} = (0, 1, 0)$ or the Neumann BC $\partial \mathbf{p} / \partial y|_{y=0,1} = (0, 0, 0)$; however, the component p_3 may be unstable to perturbations depending on the value of $\zeta(\nu + 1)$, leading to true 3D spontaneous flows. We use two initial perturbations given by the following: $\delta p_1 = \delta \sin(k\pi y)$, $\delta p_3 = \delta \sin(k\pi y)$ for the Dirichlet BC and $\delta p_1 = \delta \cos(k\pi y)$, $\delta p_3 = \delta \cos(k\pi y)$ for the Neumann BC, respectively, in our computations. Figure 19 depicts four solutions, which all show the final out-of-plane steady states at $T = 50$. We remark that in Figs. 19(c), 19(d), 19(g), and 19(f), the Neumann BC is used for \mathbf{p} , we choose appropriate values of ζ to get the spatially inhomogeneous out-of-plane structures. We point out that when $|\zeta|$ is too large, the polarity vector reaches a spatially homogeneous out-of-plane alignment, where the velocity field is essentially zero.

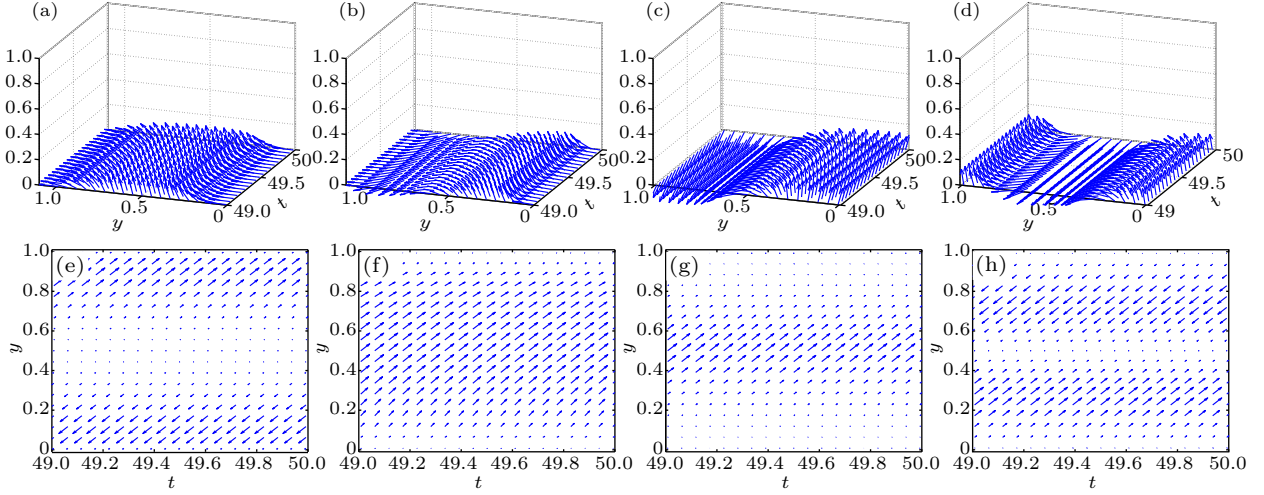


Fig. 19. Out-of-plane structures of the polarity vector and the corresponding velocity field. The parameter values are $K_1 = K_3 = 0.01, h_1 = h_2 = 10, \gamma = 1, \omega = 0, \lambda = 0, \eta = 1, \beta = 0$. The velocity field $\mathbf{v} = (v_1, v_3)$ is shown at time $T = 50$. Steady states are reached in all cases. (a)–(d) The polarity vector structure depicted in 3D. (e) The velocity near the walls flows to opposite directions. Polarity vectors exhibit strong, steady state, out-of-plane orientation. (f) The velocity flows to the same direction. Polarity vectors show two big bands of out-of-plane orientation pointing to opposite directions. (g) The velocity flows to the same direction. Polarity vectors show two big bands of out-of-plane orientation pointing to opposite directions. (h) There are two band structures. In one band the flows move in one direction while they move in the opposite direction in the other band. Polarity vectors show two bands of out-of-plane orientational patterns. The parameters are: (a) \mathbf{p} with Dirichlet BC, $\zeta = -4, v = -0.5, k = 1$, (b) \mathbf{p} with Dirichlet BC, $\zeta = -4, v = -0.5, k = 2$, (c) \mathbf{p} with Neumann BC, $\zeta = -1.8, v = -0.5, k = 1$, (d) \mathbf{p} with Neumann BC, $\zeta = -2.3, v = -0.5, k = 2$, (e) $\zeta = -4, v = -0.5, k = 1$, (f) $\zeta = -4, v = -0.5, k = 2$, (g) $\zeta = -1.8, v = -0.5, k = 1$, (h) $\zeta = -2.3, v = -0.5, k = 2$.

5.3.2. Structures under shear

For passive LC flows, the planar structures without defects are in principle stable or robust with respect to out-of-plane perturbations while those with defects tend to evolve to out-of-plane structures by evading an energy penalty. When activities are included in the model, a similar scenario remains with the Dirichlet boundary condition. Namely, when shear is weak, the active stress dominates the viscous stress, a steady structure emerges over time. While shear is strong, viscous stress dominates the active stress, the structures with defects tend to go out-of-plane to form a defect free, out-of-plane steady state.

We illustrate the result using the first initial state $\mathbf{p} = (1, \delta p_2, \delta p_3)$ next, where the perturbations are defined as $\delta p_2 = \delta \sin(k\pi y)$, $\delta p_3 = \delta \sin(k\pi y)$ for the Dirichlet BC and $\delta p_2 = \delta \cos(k\pi y)$, $\delta p_3 = \delta \cos(k\pi y)$ for the Neumann BC. The spontaneous flow structure without shear is a planar structure with these initial data and BCs. When shear is present, the planar structures of tumbling ALCs evolve to out-of-plane steady states at $T = 50$ while those of flow-aligning ALCs remain planar. Figures 20(a)–20(d) depict two steady solutions with the Dirichlet BC, where out-of-plane steady states are reached. Figures 20(e)–20(h) depict two out-of-plane steady states with the Neumann BC. The tumbling ALC goes out-of-plane at shear speed $Pe = 1$ (Figs. 20(e) and 20(f)) while the flow-aligning one stays in-plane (Figs. 20(g) and 20(h)). We remark that, for the first initial state with the Dirichlet BC or the Neumann BC, if $\zeta = 0$, p_3 is stable for small perturbations for any v under shear flow, indicating that it is the bulk active stress that triggers the out-of-plane instability, leading to a 3D

steady structure.

We then consider simulations with the second initial state $\mathbf{p} = (\delta p_1, 1, \delta p_3)$ with the Dirichlet BC $\mathbf{p}|_{y=0,1} = (0, 1, 0)$ or the Neumann BC $\partial \mathbf{p} / \partial y|_{y=0,1} = \mathbf{0}$, in which the perturbations are given above. When shear is absent, we find that the system can be unstable in p_3 direction, so that the spontaneous flow exists in 3D when $\zeta(v+1) < 0$; when $\zeta(v+1) > 0$; however, the planar structures are stable to the out-of-plane perturbation. When weak shear is present, the scenario remains. It also applies to the scenario where the Neumann BC is imposed. For strong shear flows, out-of-plane structures emerge for any ζ when the liquid crystal is a tumbler, that is, $|v| < 1$ with the Dirichlet BC or the Neumann BC.

5.3.3. Role of the active viscous stress

Finally, we consider interactions among the active viscous stress, the bulk active stress, and the shear stress. The active viscosity β is in general stabilizing in the shear flow. In the above, we mentioned that the out-of-plane structures emerge when $\zeta(v+1) < 0$ with the second initial state at $\zeta = -4, v = -0.5, Pe = 1, \beta = 0$. If we increase the active viscosity from zero to $\beta = 2$, then the structures can be limited to the 2D plane. Figure 21 depicts some solutions associated to this case. Figures 21(a)–21(c) show the out-of-plane structures and the corresponding velocity fields for $\beta = 0, 0.2, 0.5$, respectively, where velocity fields show nonzero components in v_3 and the polarity vector component p_3 is nonzero in general. Figure 21(d) depicts the planar steady state for $\beta = 2$, where the corresponding velocity field, depicted in Fig. 21(h), has a zero component $v_3 = 0$ and correspondingly $p_3 = 0$.

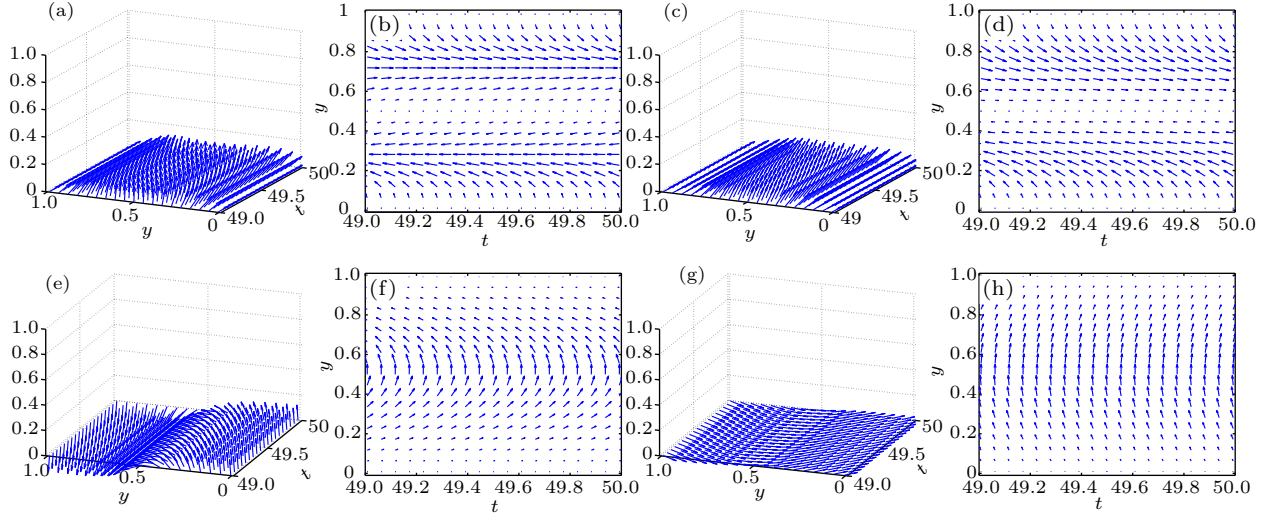


Fig. 20. Polarity vector structures and velocity field. The parameter values are $K_1 = K_3 = 0.01, h_1 = h_2 = 10, \gamma = 1, \omega = 0, \lambda = 0, \eta = 1, \beta = 0, Pe = 1$. The velocity difference $\mathbf{v} = (v_1 - Pe y, v_3)$ is drawn at time $T = 50$. (a) Out-of-plane polarity vector field is shown with strong logrolling region in the middle of the field. The velocity field difference, panel (b) shows the difference between the actual velocity field and the linear shear flow. Two bands are identified, one is faster than the shear flow field and the other is slower. (c) Polarity vector field, which tilted out-of-plane orientational field. Panel (d) shows the velocity field difference. Two bands are identified. (e) Polarity fields with nearly logrolling out-of-plane steady states near the wall. Panel (f) shows that the velocity field difference forms a single band structure. (g) Nearly planar but really out-of-plane polarity vector structure. Panel (h) depicts the velocity difference. The parameters are: (a) \mathbf{p} with Dirichlet BC, $\zeta = -4, v = 0.5, k = 1$, (b) $\zeta = -4, v = 0.5, k = 1$, (c) \mathbf{p} with Dirichlet BC, $\zeta = -4, v = -0.5, k = 1$, (d) $\zeta = -4, v = -0.5, k = 1$, (e) \mathbf{p} with Neumann BC, $\zeta = -4, v = 0.5, k = 1$, (f) $\zeta = -4, v = 0.5, k = 1$, (g) \mathbf{p} with Neumann BC, $\zeta = 8, v = -1.5, k = 1$, (h) $\zeta = 8, v = -1.5, k = 1$.

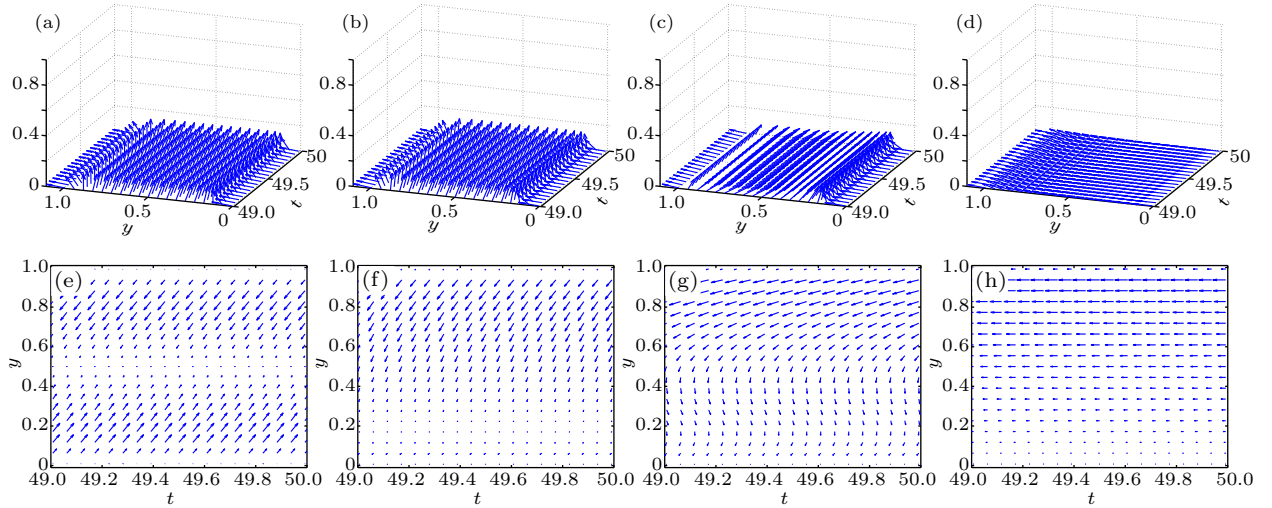


Fig. 21. Structures of tumbling ALCs with the second initial state $\mathbf{p} = (\delta p_1, 1, \delta p_3)$ and the Dirichlet BC at $\beta = 0, 0.2, 0.5, 2$. The parameter values are $K_1 = K_3 = 0.01, h_1 = h_2 = 10, \gamma = 1, \omega = 0, \lambda = 0, \eta = 1, \zeta = -4, v = -0.5, k = 1$. The velocity field $\mathbf{v} = (v_1 - Pe y, v_3)$ is shown at time $T = 50$. The shear speed $Pe = 1$. (a)–(c) Steady state out-of-plane polarity vector structures at small β . (d) Steady state planar polarity structure at large β . (e)–(h) Corresponding velocity fields. The parameters are: (a) \mathbf{p} with Dirichlet BC, $\beta = 0$, (b) \mathbf{p} with Dirichlet BC, $\beta = 0.2$, (c) \mathbf{p} with Dirichlet BC, $\beta = 0.5$, (d) \mathbf{p} with Dirichlet BC, $\beta = 2$, (e) $\beta = 0$, (f) $\beta = 0.2$, (g) $\beta = 0.5$, (h) $\beta = 2$.

Remark

(i) In most of the numerical examples presented in this paper, the ALC system chosen is a tumbler. We emphasize that flow-aligning states can also generate spontaneous flows under sufficiently strong activities. There is no qualitative difference between a defect-free spontaneous flow generated by a tumbling ALC system and the one generated by a flow-aligning ALC system. We therefore choose the tumbling system most of the time because of their more dramatic structural features over the flow-aligning ALC system.

(ii) In all of these studies, we have essentially neglected the role of the self-propelled speed ω . Our analysis and numerical computations show that its influence upon the flow and orientational structures is similar to that of β when coupled to the shear flow. It can pin the planar dynamics to the plane when the model would be unstable to the out-of-plane component without it. In fact, we notice that $(\beta(v+1)/2\eta + \omega)^2$ controls the p_3 instability in a linear stability analysis of the 1D channel flow in an inertialess model.^[56] We will pursue a comprehensive stability analysis on the full model in a sequel.

6. Conclusion

In this paper, we have systematically studied the dynamics of active polar liquid crystal systems using a polar active liquid crystal model, which extends the Ericksen–Leslie theory for passive liquid crystals, in the near hydrodynamic equilibrium situation, in the viscous stress dominated regime, and in the full model. A systematic derivation of the continuum model is conducted and its thermodynamic consistency is checked. We then carry out a linear stability analysis for constant steady states in an unbounded domain or a domain with a periodic boundary condition to study near equilibrium dynamics and to demonstrate the linear instability inherent in this model system and its dependence on model parameter values. Through the linear analysis, a complete stability diagram for two types of instabilities for a liquid crystal phase is obtained, demarcating the stable regions in a parameter space involving three key model parameters. In addition, three potentially unstable modes are identified for the isotropic state. This analysis completely characterizes the linearized stability of the ALC system with three active mechanisms included (which are: self-propelled velocity, active bulk stress, and active viscous stress), extending the analysis on the steady states in the literature and providing guidance for nonlinear simulations of the active matter system in an unbounded or a periodic domain.

We then studied the model prediction in a finite domain in 1D numerically to investigate flow-driven dynamics of the polarity vector's with a focus on the role of the activity of the polarity vector. We concentrate only on two special flow fields: the shear or Couette flow and the Poiseuille flow. For flow-aligning ALCs, the stable in-plane steady state survives the out-of-plane perturbation in both shear and Poiseuille flows. For tumbling ALCs, the planar tumbling time periodic solution is stable in shear flows only subject to the Neumann boundary condition and weak anchoring conditions. Under the Dirichlet boundary condition in shear and all the boundary conditions in the Poiseuille flow field, defects can form in the polarity vector field periodically in time in planar dynamics. These tumbling solutions are unstable with respect to the out-of-plane perturbations, such that out-of-plane steady states emerge eventually as the globally stable solutions in this model regime.

Finally, we study solutions of the full model in a 1D, finite domain numerically by demonstrating a host of interesting solution phenomena. We once again contrast the dynamics of the system with the polarity vector confined to a plane to that without any orientational constraints. We follow the nonlinear evolution of the spontaneous flow when the polarity vector is confined to a 2D plane and notice that it normally evolves into a defect free steady state without shear. When

shear is introduced, some shear-induced asymmetric, spatial-temporal structures can emerge, enriching the polarity vector patterns in space–time. These patterns depend strongly on the boundary condition, active viscous stress, and the initial state from which the system evolve. When the constraint on the polarity vector is lifted in the third dimension, some solution structures evolve into fully 3D structures while others remain planar. The factors determining the planar versus out-of-plane solution depend on the bulk active activity and geometry of the ALC molecules ($\zeta(v-1)$, $\zeta(v+1)$), active viscous stress (β), self-propelled velocity (ω), shear speed (Pe), the initial states, as well as the consistent boundary conditions. The active viscous stress and the self-propelling velocity are shown to have a tendency to favor planar dynamics. More detailed analysis on the role of the active parameters in the complete phase diagram will be carried out in a sequel.

Appendix A

The linearized system (19) is obtained as follows. For the liquid crystal state $\|\mathbf{p}_0\|^2 = (h_1 + \gamma\lambda)/h_2$, we substitute perturbation equation (18) into governing equations (16), keep the terms at the linear order of ε and neglect the high-order terms, then the linear system of the perturbation is given by

$$\begin{aligned} & \alpha \mathbf{p}_1^{(0)} + \left[\mathbf{i}(\mathbf{v}_0 + \omega \mathbf{p}_0) \cdot \mathbf{k} + \frac{K_3}{\gamma} \|\mathbf{k}\|^2 \right] \mathbf{p}_1^{(0)} \\ & - \frac{\mathbf{i}}{2}(\nu+1)(\mathbf{k} \cdot \mathbf{p}_0) \mathbf{v}_1^{(0)} + \frac{\mathbf{i}}{2}(1-\nu)(\mathbf{p}_0 \cdot \mathbf{v}_1^{(0)}) \mathbf{k} \\ & + \frac{K_1 - K_3}{\gamma} (\mathbf{k} \cdot \mathbf{p}_1^{(0)}) \mathbf{k} + \frac{2h_2}{\gamma} (\mathbf{p}_0 \cdot \mathbf{p}_1^{(0)}) \mathbf{p}_0 = 0, \\ & \alpha \mathbf{v}_1^{(0)} + \left[\mathbf{i}(\mathbf{v}_0 \cdot \mathbf{k}) + \eta \|\mathbf{k}\|^2 \right] \mathbf{v}_1^{(0)} + \mathbf{i} \mathbf{k} \Pi_1^{(0)} + S_1 \mathbf{p}_1^{(0)} \\ & + S_2 (\mathbf{k} \cdot \mathbf{p}_1^{(0)}) \mathbf{p}_0 + S_3 (\mathbf{k} \cdot \mathbf{p}_1^{(0)}) \mathbf{k} \\ & + S_4 (\mathbf{p}_0 \cdot \mathbf{p}_1^{(0)}) \mathbf{p}_0 + S_5 (\mathbf{p}_0 \cdot \mathbf{p}_1^{(0)}) \mathbf{k} = 0, \\ & \mathbf{k} \cdot \mathbf{v}_1^{(0)} = 0, \end{aligned} \quad (\text{A1})$$

where the parameters S_i ($i = 1, 2, 3, 4, 5$) are given by

$$\begin{aligned} S_1 &= \beta \|\mathbf{k}\|^2 + \mathbf{i} \left[-(\zeta + \gamma\lambda\nu) - \frac{1}{2}(\nu+1)K_3 \|\mathbf{k}\|^2 \right] (\mathbf{k} \cdot \mathbf{p}_0), \\ S_2 &= \mathbf{i} \left[-(\zeta + \gamma\lambda\nu) - \frac{1}{2}(\nu-1)K_1 \|\mathbf{k}\|^2 \right], \\ S_3 &= \beta - \frac{\mathbf{i}}{2}(\nu+1)(K_1 - K_3)(\mathbf{k} \cdot \mathbf{p}_0), \\ S_4 &= -2\mathbf{i}\nu h_2 (\mathbf{k} \cdot \mathbf{p}_0), \\ S_5 &= \mathbf{i}(h_1 - h_2 \|\mathbf{p}_0\|^2). \end{aligned}$$

We rewrite the linear system into the matrix form

$$\left(\begin{pmatrix} 0 & 0 & 0 \\ 0 & \alpha \mathbf{I} & 0 \\ 0 & 0 & \alpha \mathbf{I} \end{pmatrix} + \begin{pmatrix} 0 & 0 & \mathbf{k} \\ 0 & A & B \\ \mathbf{i} \mathbf{k}^T & C & D \end{pmatrix} \right) \begin{pmatrix} \Pi_1^{(0)} \\ \mathbf{p}_1^{(0)} \\ \mathbf{v}_1^{(0)} \end{pmatrix} = 0, \quad (\text{A2})$$

where the components of the matrices are

$$A = \left[\mathbf{i}(\mathbf{v}_0 + \omega \mathbf{p}_0) \cdot \mathbf{k} + \frac{K_3}{\gamma} \|\mathbf{k}\|^2 \right] \mathbf{I} + \frac{K_1 - K_3}{\gamma} \mathbf{k} \mathbf{k} + \frac{2h_2}{\gamma} \mathbf{p}_0 \mathbf{p}_0,$$

$$B = -\frac{i}{2}(\nu + 1)(\mathbf{k} \cdot \mathbf{p}_0)\mathbf{I} + \frac{i}{2}(1 - \nu)\mathbf{k}\mathbf{p}_0,$$

$$C = S_1\mathbf{I} + S_2\mathbf{p}_0\mathbf{k} + S_3\mathbf{k}\mathbf{k} + S_4\mathbf{p}_0\mathbf{p}_0 + S_5\mathbf{k}\mathbf{p}_0,$$

$$D = [i(\mathbf{v}_0 \cdot \mathbf{k}) + \eta\|\mathbf{k}\|^2]\mathbf{I},$$

and \mathbf{I} is the 3×3 unit matrix. We then solve this linear system (A2) for the eigenvalues (growth rates).

References

- [1] Toner J and Tu Y 1995 *Phys. Rev. Lett.* **75** 4326
- [2] Toner J and Tu Y 1998 *Phys. Rev. E* **58** 4828
- [3] Ramaswamy S, Simha R A and Toner J 2003 *Europhys. Lett.* **62** 196
- [4] Narayan V, Ramaswamy S and Menon N 2007 *Science* **317** 105
- [5] Koch A J and Meinhardt H 1994 *Rev. Mod. Phys.* **66** 1481
- [6] Budrene E O and Berg H C 1991 *Nature* **349** 630
- [7] Budrene E O and Berg H C 1995 *Nature* **376** 49
- [8] Liverpool T B 2003 *Phys. Rev. E* **67** 031909
- [9] Matsushita M 1997 *Bacteria as Multicellular Organisms* (New York: Oxford: Oxford University Press)
- [10] James D M 2002 *An Introduction To Mathematical Biology* (New York: Springer-Verlag)
- [11] Timothy R K, Walter F P, Thomas E M and Sen A A 2005 *Chem. Int. Ed.* **117** 754
- [12] Dombrowski C, Cisneros L, Chatkaew S, Goldstein R E and Kessler J O 2004 *Phys. Rev. Lett.* **93** 098103
- [13] Kruse K, Joanny J F, Jülicher F, Prost J and Sekimoto K 2004 *Phys. Rev. Lett.* **92** 078101
- [14] Kruse K, Joanny J F, Jülicher F, Prost J and Sekimoto K 2005 *Eur. Phys. J. E* **16** 516
- [15] Joanny J F, Jülicher F, Kruse K and Prost J 2007 *New J. Phys.* **9** 422
- [16] Wang Q, Yang X, David A, Elston T, Jacobson K, Maria M and Forest M G 2012 *Computational and Modeling Strategies for Cell Motility: Bacteria as Multicellular Organisms* (New York: Springer)
- [17] Ramaswamy S 2010 *Annu. Rev. Condens. Matter Phys.* **1** 323
- [18] Marchetti M C, Joanny J F, Ramaswamy S, Liverpool T B, Prost J, Rao M and Simha R A 2013 *Rev. Mod. Phys.* **85** 1143
- [19] Simha R A and Ramaswamy S 2002 *Phys. Rev. Lett.* **89** 058101
- [20] De-Gennes P G and Prost J 1993 *The Physics of Liquid Crystals* (Oxford: Oxford Science Publications)
- [21] Gruler H, Dewald U and Eberhardt M 1999 *Eur. Phys. J. B* **11** 187
- [22] Kemker R, Kling D, Kaufmann D and Gruler H 2000 *Eur. Phys. J. E* **1** 215
- [23] Vicsek T, Czirók A, Ben-Jacob E, Cohen I and Shochet O 1995 *Phys. Rev. Lett.* **75** 1226
- [24] Baskaran A and Marchetti M C 2012 *Eur. Phys. J. E* **35** 95
- [25] Saintillan D and Shelley M J 2008 *Phys. Rev. Lett.* **100** 178103
- [26] Liverpool T B and Marchetti M C 2006 *Phys. Rev. Lett.* **97** 268101
- [27] Baskaran A and Marchetti M C 2008 *Phys. Rev. Lett.* **101** 268101
- [28] Baskaran A and Marchetti M C 2009 *Proc. Natl. Acad. Sci. USA* **106** 15567
- [29] Petitjean L, Reffay M, Grasland-Mongrain E, Poujade M, Ladoux B, Buguin A and Silberzan P 2010 *Biophys. J.* **98** 1790
- [30] Peruani F, Starruss J, Jakovljevic V, Anderseng L S, Deutsch A and Bär M 2012 *Phys. Rev. Lett.* **108** 098102
- [31] Mishra S, Baskaran A and Marchetti M C 2010 *Phys. Rev. E* **81** 061916
- [32] Voituriez R, Joanny J F and Prost J 2005 *Europhys. Lett.* **70** 404
- [33] Saintillan D and Shelley M J 2007 *Phys. Rev. Lett.* **99** 058102
- [34] Saintillan D and Shelley M J 2008 *Phys. Fluids* **20** 123304
- [35] Hohenegger C and Shelley M J 2010 *Phys. Rev. E* **81** 046311
- [36] Kanevsky A, Shelley M J and Tornberg A K 2010 *J. Comput. Phys.* **229** 958
- [37] Baskaran A and Marchetti M C 2010 *J. Stat. Mech.* **2010** 04019
- [38] Liverpool T B, Marchetti M C, Joanny J F and Prost J 2010 *Europhys. Lett.* **85** 18007
- [39] Gopinath A, Hagan M F, Marchetti M C and Baskaran A 2012 *Phys. Rev. E* **85** 061903
- [40] Forest M G, Zhou R and Wang Q 2013 *Soft Matter* **21** 5207
- [41] Baskaran A and Marchetti M C 2008 *Phys. Rev. E* **77** 011920
- [42] Rey A D 2007 *Soft Matter* **3** 1934
- [43] Ae-Gyeong C and Rey A D 2001 *Phys. Rev. E* **64** 041701
- [44] Justin S B, Frank J and Stephan W G 2011 *Phys. Rev. Lett.* **106** 028103
- [45] Giomi L and Marchetti M C 2012 *Soft Matter* **8** 129
- [46] Edwards S A and Yeomans J M 2009 *Europhys. Lett.* **85** 18008
- [47] Elgeti J, Cates M E and Marenduzzo D 2011 *Soft Matter* **7** 3177
- [48] Giomi L, Liverpool T B and Marchetti M C 2010 *Phys. Rev. E* **81** 051908
- [49] Giomi L, Marchetti M C and Liverpool T B 2008 *Phys. Rev. Lett.* **101** 198101
- [50] Forest M G, Phuworawong P, Wang Q and Zhou R 2014 *Philosophical Transactions of the Royal Society A* (in press)
- [51] Martin P C, Parodi O and Pershan P S 1972 *Phys. Rev. A* **6** 2401
- [52] Leslie F M 1979 *Theory of Flow Phenomena in Liquid Crystals* (New York: Academic Press)
- [53] Chandrasekhar S 1992 *Liquid Crystals* (Cambridge: Cambridge University Press)
- [54] Liverpool T B and Marchetti M C 2008 *Hydrodynamics and Rheology of Active Polar Filaments* (New York: Springer) p. 177
- [55] Forest M G, Wang Q and Bechtel S E 1997 *Physica D: Nonlinear Phenomena* **94** 527
- [56] Yang X and Wang Q 2014 (Preprint)